U.S.G.S. Earthquake Hazards Program Final Technical Report for External Research Support

U.S.G.S. Award Number: Collaborative Award G15AP00080 and G15AP00081

Title of Award: The Hydrologic Connection Between Basal Reservoir Injection, Micro/Mesoscale Crystalline Basement Fault Zones, and Induced Seismicity: Collaborative Research with utah state university and new Mexico tech

Principal Investigators:

Dr. James P. Evans and Dr. Kelly K. Bradbury Dept. of Geology, Utah State University, 4505 Old Main Hill Logan, UT 84322-4505 435-797-1267; 435-797-1588 fax; james.evans@usu.edu; Kelly.bradbury@usu.edu

Dr. Mark Person and Dr. Peter Mozley Dept. of Earth and Environmental Science, New Mexico Tech, 801 Leroy Place, Socorro, NM 87801; markaustinperson@gmail.com; psmozley@gmail.com

Award Term: January 1, 2015 – May 31, 2017

Abstract

We investigate the range of rock properties and spatial heterogeneity at the Precambrian nonconformity zone in a variety of sites in the central U. S. and Wyoming, using outcrop and core analogs, and examine how the geology of the nonconformity zone may influence fluid flow. Our methods of analyses include mapping of lithologies and deformation structures, petrographic and microstructural analysis, and geochemical analysis of rocks. We infer the nature of fluid flow in the past and make predictions about fluid flow in the future. In addition, this information is used to inform hydrological models, improving the ability to refine seismic hazard models associated with wastewater injection.

Based on our observations at multiple outcrop localities and in several drill cores, we identify and characterize three common geological scenarios encountered at the nonconformity. These consist of the presence of: 1) basal conglomerate, 2) weathered/altered horizon, and 3) mineralized contacts. These scenarios, or combinations thereof, may be fractured or faulted, resulting in a variety of hydrological consequences. The permeability of basal conglomerates and weathered horizons at the contact is texturally and mineralogically dependent. Regolith, clast-supported grus or granitic wash, or poorly cemented conglomeratic horizons may act as high permeability conduits, whereas a clay-rich matrix-supported grus or granitic wash, or tightly cemented conglomerate, may act as low permeability barriers. Mineralized contacts may act as low permeability barriers due to a reduction of pore space and/or resistance to weathering. The introduction of modern warm brines of complex or mixed geochemistries during injection may result in mineralization or chemical alteration, dynamically affecting permeability over time and space depending on the mineralogy of the host rock and chemical composition of the injected brine.

We used hydrogeologic models to assess how fault-zone architectural components (i.e. fault core and damage zones) and properties of weathered zones influence the downward propagation of fluid pressures into the crystalline basement. We found that realistic, multicomponent representations of conduit-barrier fault zones were able to effectively transmit elevated pore pressures to depths of ~2.5 km within the crystalline basement while still compartmentalizing fluid flow within the injection reservoir. Furthermore, our results indicate that the presence of a laterally continuous, relatively low-permeability altered/weathered basement horizon ($k_{\text{weathered layer}} = 0.1 \times k_{\text{basement}}$) can reduce the penetration depth of the same pressure front to ~500 m. Permeability enhancement via hydromechanical failure was found to increase depth of pressure front migration by factors of 1.25 to 4 depending on the assigned values of enhancement parameters. We also constructed hydrologic models to explore the potential linkages between oil-field brine reinjection and increases in earthquake frequency (up to M_d 3.26) in southeastern New Mexico and to assess different injection management scenarios aimed at reducing the risk of triggered seismicity. Our analysis focused on saline water re-injection into the basal Ellenburger Group beneath the Dagger Draw Oil field, Permian Basin.

Introduction

Deep wastewater injection from oil and gas operations helps prevent the contamination of water resources at the Earth's surface and in the unsaturated zone. However, injecting large volumes of fluids may accelerate injection induced seismicity. Over the past 20 years, the central United States has experienced an increase in the rate of seismic activity (Fig. 1). The central United States is thought to be a 'tectonically quiet' region, in which intraplate strain rates are low (<10⁻¹⁷ sec⁻¹) (Calais et al., 2006; Dixon et al., 1996), fault slip rates are slow (<<1 mm/yr) (Harrison et al., 1999), recurrence intervals of intraplate earthquakes are long (104-105 yrs.) (Crone et al., 2003), and fault slip may occur on ancient 'hidden' faults not seen in historic seismic records. The high rates of current seismic activity have motivated numerous studies investigating the causes for these earthquakes. Determining whether the increased seismic activity in the midcontinent U.S. is a product of deep wastewater injection, or natural tectonic activity, requires an understanding of the subsurface geology and any possible fluid-pressure pathways that may exist near injection sites. Numerous multidisciplinary studies explore a range of questions surrounding injection-related seismicity to better understand the processes involved in induced seismicity via deep wastewater injection. Recent observations suggest that deep wastewater injection is the culprit (Ellsworth, 2013; Keranen et al., 2014; Weingarten et al., 2015; Yeck et al., 2016; Walsh and Zoback, 2015; Zhang et al., 2013).

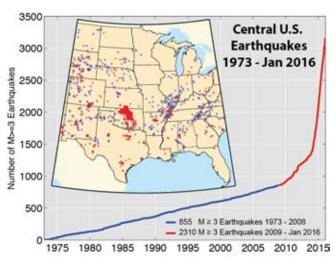


Fig. 1: The midcontinent United States has seen a rapid increase in the number of M 3+ earthquakes over the past decade. This rapid increase in seismic activity rate began around 2009, and has been attributed to the wastewater disposal via Class II injection wells. From the U.S. Geological Survey Earthquake Hazards Program webpage (accessed in June, 2017).

The total number of Class II wells in the United States is reported to be between 140,000 and 160,000 as of 2013 (Evans et al., 2013), of which ~16,000 of these wells are active brine disposal wells and 3,400 inject fluids at depths of >1.8 km (Evans et al., 2013). Wastewater injection occurs on a large scale, with the volume of brine disposed in Oklahoma alone in 2015 > 2.7 million barrel per day (Murray, 2016). Injection rates in individual wells range between ~100 (bbl/month) to up to 2 million bbl/month (Weingarten et al., 2015). The majority of these active brine disposal wells are in oil and gas basins in Oklahoma, Texas, Kansas, and Wyoming (Fig. 2; Weingarten et al., 2015).

Other regions experiencing high rates of induced seismicity include west Texas, southeastern Colorado, central Arkansas, southern Illinois, and northern and southeastern New Mexico. Previously, northeastern Ohio experienced seismicity due to injection into sandstone intervals in the Knox Dolomite and in the Mt. Simon Sandstone (Kim, 2013), however, deep injection has ceased due to successful mitigation efforts by the state following a M 4.0 earthquake in December, 2011. Mitigation efforts included: 1) shutting down the injection

well associated with seismicity and surrounding injection wells; 2) prohibiting the drilling of Class II injection wells into Precambrian basement rock, 3) changing the volumes of injection in a well; and 4) increasing supplemental site assessment documents required to obtain a permit (National Technical Workgroup and Underground Injection Control, 2014). Areas with large numbers of brine disposal wells (North Dakota, the Michigan Basin, large areas of Texas and Louisiana Gulf Coast) are not affected by induced seismicity, indicating that region-specific subsurface geology and in-situ stress states may be a controlling factor in the fate of brine disposal.

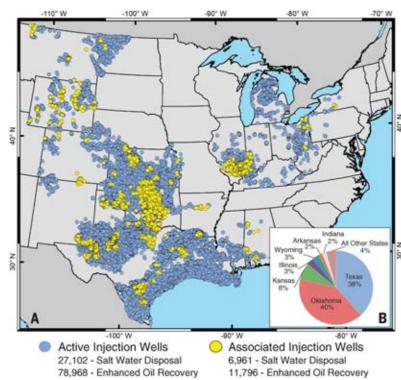


Fig. 2: (A) Map showing the location of active class II injection wells in the central eastern United States (CEUS). Active injection wells from the database are shown as blue circles. Spatiotemporally associated injection wells, defined as those within a 15km radius and active at the time of an earthquake, are shown as yellow circles. The CEUS region comprises all states intersected by 109°W longitude and eastward. The total number of wells, including inactive or abandoned wells the CEUS, is 188,570. Of the 18,757 associated injection wells, >77% are currently active. (B) The inset pie diagram shows

spatiotemporally associated injection wells by state. Only 8% of all injection wells are located in Oklahoma, but 40% of the associated injection wells in the CEUS are located in Oklahoma. From Weingarten et al. (2015).

Geologic and Hydrologic Setting of Midcontinent Brine Injection

Many brine disposal wells are completed into basal (Cambro-Ordovician) sedimentary reservoirs near Precambrian crystalline basement rock (Murray, 2015). The Cambro-Ordovician Arbuckle Formation is the target disposal zone for ~50% of injection wells in Oklahoma and Kansas (Murray, 2015). Other target formations include the Cambrian Mt. Simon Sandstone, the Cambro-Ordovician Knox Group, and the lower Ordovician Ellenberger Group. Basement rocks in the midcontinent primarily consist of granite, rhyolite, and varying grades of metamorphic rocks (Denison et al., 1984). The contact between the sedimentary rocks and crystalline igneous and metamorphic rocks in the central United States forms the subsurface nonconformity contact of the region (Sloss, 1963). Fault zones in the midcontinent are not commonly exposed at the surface, and typically penetrate basement, dip steeply, and follow two dominant trends: east-west to northwest-southeast, and north-south to northeast-southwest (Marshak and Paulsen, 1996) (Fig. 3). The surface of the nonconformity in the midcontinent has a structural relief of 1 to 5 km, and lies between

0.5 to ~8 kilometers below sea level (Marshak and Paulsen, 1996; Marshak et al., 2017) (Fig. 3).

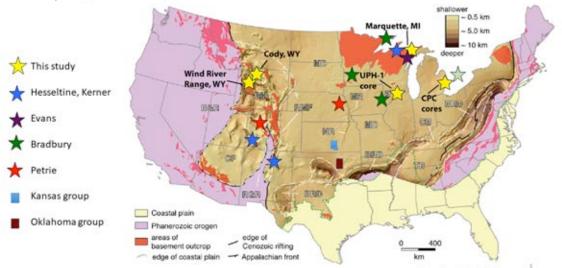


Fig. 3: Digital elevation model of the Great Unconformity (United States), in shaded relief. Brown areas represent cratonic platform crust of the continent. The map shows the locations of major faults and folds, as well as the locations of nonconformity analogs examined as part of this study (yellow stars) and other studies. Modified from Domrois et al. (2015) and Marshak et al. (2017).

Earthquakes associated with deep wastewater injection are typically small magnitude events occurring at depths of >1.8 km, nucleating on basement-hosted faults up to 20 km away from the injection point (Keranen et al., 2014; Zhang et al., 2013, 2016). Although most earthquakes are small, induced seismic events have potential to be damaging, with notable events including the 2011 M 5.7 Prague, OK earthquake; the 2014 Guthrie, OK earthquakes (33 M3+ events); the 2014 M 4.9 Milan, KS earthquake; the 2011 M 5.3 Trinidad, CO earthquake; the 2011 M 4.8 Fashing, TX earthquake; the 2011 M 4.7 Guy, AR earthquake; the 2011 M 3.9 Youngstown, OH earthquake; among others (Kim, 2013). Recently, Oklahoma has experienced a total of 623 M3+ earthquakes in 2016, including one M 5.8 near Pawnee, OK (Earthquake Top Ten and Yearly Summaries, http://www.ou.edu/content/ogs/research/earthquakes/Information.html).

The mechanics of injection related to seismicity is linked to increased pore fluid pressures associated with subsurface injection (National Research Council, 2013). Injection-related seismicity nucleates on deep basement faults that may be up to 15 km or more from the injection point (Keranen et al., 2014; Zhang et al., 2016). Seismic events may occur months to a few years after injection, indicating that fluid pressure must be traveling along relatively fast hydrological pathways between the injection point and the faults that slip. The propagation of pore fluid pressure from the injection point to basement-hosted faults can modify the stress state of the fault, causing failure, ultimately resulting in seismic activity (National Research Council, 2013). Geologically reasonable fast paths include connected fracture and fault networks or the Precambrian nonconformity zone, which lies in proximity to most injection points. The Precambrian nonconformity, commonly known as The Great Unconformity, is a globally occurring stratigraphic surface that represents a gap in time of 0.7 to > 2.0 Ga, a time during which exposed crystalline rock may have become deeply weathered, or partially eroded (Dutton, 1882). The subsequent basal Cambrian transgression may have acted as a 'wave-based razor', removing the deeply weathered surface of the exposed crystalline rock, exposing fresh crystalline rock that was subjected to rapid weathering rates during the early Cambrian (Peters and Gaines, 2012).

Geologic Methods We implement a multi-scaled approach to document variations in the structure and composition and structural and permeability architecture of nonconformity zones. The methods listed below are employed at each site, where applicable.

Mapping of lithologic and brittle deformation features at the map, outcrop, and core scales allows us to document the geometry of the contact, determine the relationship of faults and fractures to the contact, and to examine lithologic variations in relation to the contact and brittle deformation features. We use outcrop-scale cross-sectional mapping (scales of 1:500 to 1:7,000) to determine the sinuosity of the contact, the nature and distribution of the rocks along the nonconformity, and the distribution and nature of fracture and fault networks. The mapping also enables us to locate key samples for further analyses. We create lithologic columns in core and in outcrop to document meter-scale variations in lithology and textures seen vertically through the contact. Fracture transects on the outcrop and map scale reveal the orientations and intensities of fracture sets and how they may relate to faults or fault zones, providing us insight into potential conduit systems in the nonconformity zone. Core from the UPH-1 drill hole (Coates et al., 1983) was examined at the

Wisconsin Geological & Natural History Survey Research Collections and Education Center in Mt. Horeb, Wisconsin, in June of 2016. The CPC BD-139 and CPC BD-151 cores were examined and sampled at the Michigan Geological Repository for Research and Education in Kalamazoo, Michigan. Core analyses consists of photography, lithologic logging with special attention to weathering and alteration horizons, noting of fractures and faults where applicable, and sampling of host rocks, alteration, fault or fracture surfaces, and contact rocks. In addition to core analyses, we use the legacy data provided by the core repositories, which provide permeability and porosity measurements. The data for CPC BD-151 and CPC BD-139 were collected in 1971 by Maness Petroleum Laboratories, in Mt. Pleasant, Michigan, using standard laboratory methods at the time. A total of 58 standard uncovered 30 µm thick thin sections from the outcrop and core localities were examined. X-ray diffraction analysis was performed on a total of 100 samples or subsamples. Sample preparation and analysis was done in house at the Utah State University Geology Department.

Geology of Core and Outcrop Study Sites

We examined sites that sample a range of geological properties that may exist at the contact, enabling us to document end-member geological scenarios (Error! Reference source not found.). Exposures of the nonconformity in the areas affected by induced seismicity are rare, and core capturing the nonconformity zone is not widely available, therefore, we look to other parts of the country for workable sites where the nonconformity is exposed at the surface, and to drill holes near depths of ~2-3 km to sample the nonconformity.

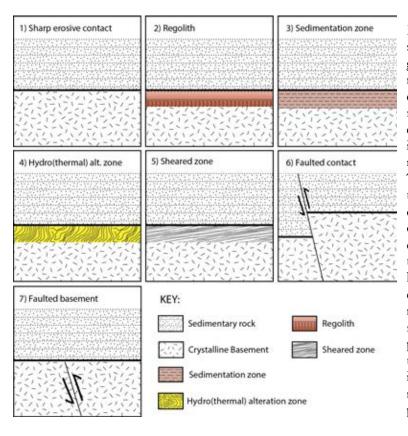
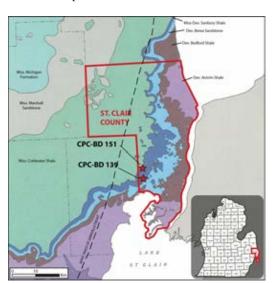


Fig. 4: Conceptual models showing a range of geological scenarios that may exist at the contact at depth. Models 1, 6, and 7 represent the standard depictions of the contact most hydrological models of deep injection. The basis of this work is that we predict that the contact is a geologically complex zone, and may exhibit one or more of the scenarios presented here. The characteristics exhibited at the contact may have implications for relative porosity permeability parameters, therefore may play an important role in fluid migration and pore fluid pressure transmission.

Core Analogs: CPC BD-139, CPC BD-151

The CPC-BD-139 and CPC BD-151 cores were sampled from selected intervals of brine disposal wells drilled for the Consumers Power Company in 1964. The drill holes are located



in St. Clair County, Michigan, at the southeastern edge of the Michigan basin (Fig. 5). The cores are stored at the Michigan Geological Repository for Research and Education (MGRRE), in Kalamazoo, Michigan, and were logged and sampled in June 2015. The majority of work for this project was done on the CPC BD-139 core.

Fig. 5: Geologic map showing the locations of the CPC BD-139 and CPC BD-151 drill holes, St. Clair County, Michigan. Modified from Milstein (1987).

The CPC BD-139 core reaches a total depth of 1412 meters, and contains the section of rock that lies between the Mississippian Sunbury Formation through Precambrian gneiss. We examine the section of core between 1404.5-1412 m depth, which captures the contact between the Mt. Simon Sandstone and Precambrian gneiss. The ~10 meters of the CPC BD-151 core that was

examined also captures the contact between the Mt. Simon Sandstone and Precambrian gneiss, however, the depths indicated on the core boxes are unclear.

The Cambrian Mt. Simon Sandstone in the Michigan Basin is characterized as a porous (5-15% pore space) arenite to sub-arkosic sandstone (Leeper et al., 2012). Permeability in the basal Mt. Simon Sandstone is reported to be between 1x10⁻¹⁶ m² to 1x10⁻¹² m² (Frailey et al., 2011). The Precambrian gneiss captured in this core correlates to the Grenville Front Tectonic Zone, and is characterized as granitic to tonalitic gneiss (Easton and Carter, 1995). The permeability of a typical crystalline basement rock (unfractured) is between 1x10⁻¹⁸ m² to 1x10⁻¹³ m² (Brace, 1984). The Michigan Basin is a thermally complex intracratonic basin situated over the lower peninsula of Michigan. Unexpectedly high levels of thermal maturity in the Paleozoic strata of the basin is thought to be attributed to elevated basal heat flow occurring up until Silurian time, as well as the prior existence of ~2 km of Pennsylvanian and Permian strata that has since been eroded (Everham and Huntoon, 1999).

Core Analog: UPH-1

The UPH-1 core (Fig. 6; Stephenson County, Illinois) is one of three engineering test holes drilled in the late 1970's by Commonwealth Edison as part of the Illinois Deep Hole Project (Vitaliano et al., 1986). The project was part of a feasibility study for an underground pumped hydroelectric (UPH) storage plant. UPH-1 reaches a total depth of 639 meters. The core is housed at the Wisconsin Geological & Natural History Survey Research Collections and Education Center, in Mount Horeb, Wisconsin. We logged and sampled the core in June 2016, with a focus on the section of core between 593-616 meters depth, which captures the contact between the Cambrian Mt. Simon Sandstone and Precambrian granite.

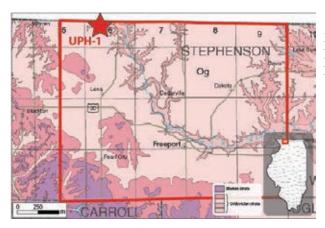


Fig. 6: Geologic map of Stephenson County, Illinois, and location of the UPH-1 drill hole. Modified from Kolata (2005).

The Mt. Simon Sandstone in this area is a medium and coarse-grained, sub- to well-rounded and moderately to well sorted arenitic to sub-arkosic sandstone. Permeability in the basal Mt. Simon Sandstone is reported to be between 1x10⁻¹⁶ m² to 1x10⁻¹² m² (Frailey et al., 2011). The Mt. Simon Formation may also include mudstones and fine-grained sandstones, and conglomeritic sandstones (Duffin, 1989; Bowen et al., 2011).

The Precambrian basement rocks in northern Illinois are part of a vast felsic igneous terrane which spans across much of the midcontinent. The basement rocks sampled by the UPH cores correlate to the Wisconsin Arch, and are characterized as alkali granites of the Mazatal Province (Whitmeyer and Karlstrom, 2007) (Error! Reference source not found.). The permeability of a typical crystalline basement rock (unfractured) is between 1x10-18 m² to 1x10-13 m² (Brace, 1984). Geochronological studies on the UPH core basement rock samples indicate an age range of 1450-1500 My (Coates et al., 1983).

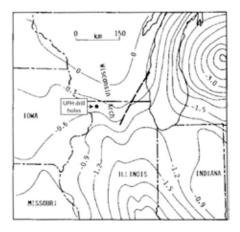


Fig. 7: Approximate topography of top of Precambrian basement for region around Commonwealth Edison drill holes. Numbers give elevation in kilometers relative to sea level. Circle in NW Illinois gives approximate location of UPH-1 and other engineering test holes. Near the drill holes the top of the basement is approximately 0.6 km deep. Adopted from Coates et al., 1983.

Outcrop Analogs: Marquette, Michigan

The southern shoreline of Lake Superior in the greater Marquette area of Michigan's Upper Peninsula exposes the Precambrian nonconformity in several areas (Fig. 8). We examine outcrops along the western shore of Presque Isle, located about 4.5 kilometers north of the town of Marquette, MI, and at Hidden Beach and Little Presque Isle, accessed from Wetmore Landing (approximately 464253E, 5163278N, UTM Grid 16T) (Fig. 8). The contact between the late Proterozoic (~1.1 Ga) Jacobsville Sandstone and Archean serpentinized peridotites is exposed along the entire western shore of Presque Isle. The contact between the Jacobsville Sandstone and the Archean Compeau Creek Gneiss of the Superior Province is marginally exposed at Hidden Beach (Fig. 8).

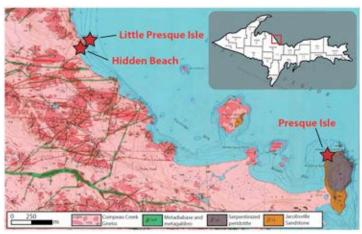


Fig. 8: Geologic map of the Marquette, Michigan field area, showing locations of Hidden Beach and Presque Isle. Modified from Gair and Thaden (1968).

The Jacobsville Sandstone is a red to reddish-brown fine- to medium grained subarkosic sandstone, becoming more arkosic near the contact with Archean basement rocks. The red is attributed to the presence of magnetite, ilmenite, and hematite, which compose 50-80% of the heavy minerals in the Jacobsville Sandstone. Grains are cemented by fine quartz mixed with clays, iron oxide, authigenic quartz, and calcite (Hamblin, 1958). Bleaching patterns occur along sub-vertical fractures and bedding planes, or other areas of increased permeability (Gair and Thaden, 1968a). The average permeability for the Jacobsville Sandstone is ~8x10-9 m² (Heinrich, 2001).

The Archean serpentinized periodotite exposed at Presque Isle exhibits blocky jointing patterns, as well as a network of stockwork quartz and carbonate veinlets in varying abundances (Gair and Thaden, 1968a). Permeability measurements are not available for the

Presque Isle serpentinized peridotite, however, the permeability of serpentinite is estimated to be between $1x10^{-22}$ m² to $1x10^{-19}$ m² (Kawano et al., 2011).

The geologic history of the Presque Isle serpentinized peridotite is not well constrained. Early research by Wadsworth (1884) believed that the peridotite intruded into Paleozoic sandstone, however, fragments of oxidized peridotite within the Jacobsville sandstone were reported by Van Hise and Bayley in 1897 (Gair and Thaden, 1968a). The most recent consensus is that the Presque Isle peridotite intruded after post-Animikie, pre-Keweenawan metamorphism (between 1.8-1.1 Gya), and was partially serpentinized at the time (Gair and Thaden, 1968a). Three metasomatic events have altered the original peridotite. The first phase of alteration is extensive serpentinization of the peridotite. Quenching of a peridotite transforms olivine and pyroxene to serpentine-group minerals and ferrous and ferric iron minerals. Volume change associated with serpentinization forms fracture networks resulting in stockwork serpentine veining (O'Hanley, 1992). The second phase of alteration is the calcium carbon dioxide metasomatism of serpentine veins, resulting in the replacement of serpentine-group minerals with dolomite, calcite, and quartz. Lastly, the interaction of surface waters and the dolomitized serpentinized peridotite resulted in dissolution and removal of carbonate minerals, leaving behind a quartz-rich regolith (Lewan, 1972).

The Archean Compeau Creek Gneiss is characterized as light-colored tonalite and granodiorite gneiss, including dark chloritic, biotitic, amphibolitic, and hornblendic varieties. It is described as largely foliated, however, rarely folded (Gair and Thaden, 1968a). The permeability of a typical crystalline basement rock (unfractured) is between 1x10⁻¹⁸ m² to 1x10⁻¹³ m² (Brace, 1984)

Outcrop Analog: Cody, Wyoming

The contact between Precambrian granite and the Cambrian Flathead Sandstone is exposed in outcrops located 10 km west of Cody, WY on US-20, at approximately $645326~{\rm E},\,4930046~{\rm N}$ (

). The exposures lie in the hanging wall block of Rattlesnake Mountain, located in the western part of the Bighorn Basin, in the Sevier-Laramide foreland (Beaudoin et al., 2012). The area is structurally characterized by steeply dipping NW-striking basement faults and moderately dipping secondary reverse faults that localize deformation in the basement rocks (Beaudoin et al., 2012) (

).

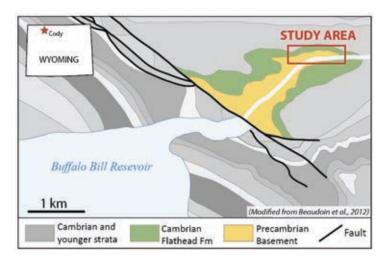


Fig. 9: Generalized geologic map of the Cody, Wyoming field area. Modified from Beaudoin et al. (2012).

The basal Cambrian Flathead Sandstone is characterized by cross-stratified, medium-grained, texturally mature orthoquartzite sandstone, often cut by channels. Local variation of this lower unit includes shaley or conglomeritic characteristics at the base, occasionally transitioning to a highly weathered zone at the top of the Precambrian (Bell and Middleton, 1978). Permeability measurements for the Flathead Sandstone are not publicly available, however, the Flathead Sandstone is commonly known to be a highly permeable, productive formation (Cooley, 1986). The Precambrian basement in this area is predominantly characterized as a coarse-grained alkali granite with mafic intrusions.

ResultsResults of the analyses of structure, mineralogy, and geochemistry from core and outcrops of the nonconformity zone are presented from the four sites described above. The types of results presented for each site depend on the methods that were able to be performed at that site. Where available permeability and porosity data collected from the borehole at the time of drilling are shown. Key data include; complete catalogs of core legacy data, thin section microphotographs, X-ray diffraction sample reports, and geochemical raw data files, are compiled in electronic appendices.

We use the term 'regolith' to describe bedrock which has been altered by processes at or near the surface, consistent with Pain (1991). This definition of regolith does not imply lithology. Grus here describes a coarse-grained felsic crystalline rock that has been subject to some degree of weathering, resulting in a poorly sorted, relatively incohesive, and typically clay-rich, horizon (Migon and Thomas, 2002). Grus is technically a type of regolith, however, the specific parent rock lithology and associated clay minerals implied by the definition have specific implications for permeability, therefore, we discuss grus and regolith separately. We use the term 'granitic wash' to refer to rock that is compositionally approximately the same as the underlying host rock, but has experienced at least a small amount of transport and deposition (Pettijohn et al., 2012). We use the term 'altered' to describe rock that varies chemically from the host rock.

Boreholes CPC BD-139, CPC BD-151

A total of 16 samples over a depth of 7.9 meters were obtained from the CPC BD-139 core. Sample numbers reflect the depth (in feet) at which the samples were taken. The logged section of the CPC BD-139 core includes one meter of Mt. Simon Sandstone and 6.7 meters of Precambrian gneiss. Five main lithologic units were identified, including sandstone, dolomitized and undolomitized finely foliated gneiss, and dolomitized and undolomitized gneiss with sub-horizontal white veins. A sharp contact separates the Mt. Simon Sandstone and the Precambrian gneiss (Fig. 10a), where the uppermost 10 cm of basement rock is a tan, fine-grained, laminated horizon containing fragmented pinkish-white carbonate veins. This horizon grades over >5 cm into a dark green, finely foliated gneiss with pink sub-vertical fractures that continues for about 1.5 meters below the contact (Fig. 10a). The finely foliated gneiss gradually grades into a dark gray gneiss with sub-horizontal pinkish-white veins, which extends through the bottom of the logged section (Fig. 10b).

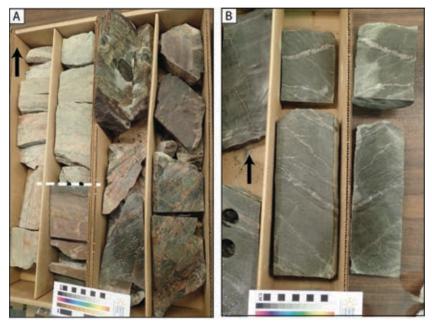


Fig. 10: Photographs of the CPC BD-139 core. Black arrows indicate up-direction. (A) Core between ~1404.5-1405.5 meters. The white dashed line marked the contact between the Cambrian Mt. Simon Sandstone (light tan) and the underlying Precambrian gneiss. The gneiss at the contact is fine-grained, tan, and dolomitized. This is underlain by green altered gneiss with sub-vertical pink-coated fractures. This lithology grades into a dark gray gneiss with sub-horizontal white veins (B, core between 1411.5-1412.5 meters), which extends through the bottom of the logged section.

Petrographic Analysis

A total of 18 thin sections from 16 samples from the CPC BD-139 core were analyzed (Appendix B). The basal Mt. Simon Sandstone contains rounded to sub-rounded, moderate to well sorted fine to coarse silica-cemented quartz grains. Graded beds (~1 cm thick) are recognizable in one of the two thin sections. Blue epoxy on sample 4607 reveals a porosity of ~5-7% (Fig. 11a).

Thin sections of the uppermost 10 cm of basement rock directly at the contact reveal very fine-grained sub-angular quartz grains supported by a tan, very fine-grained, dolomitic matrix (Fig. 11b). The concentration of quartz grains is variable, forming patches, laminations, and ptygmatic folds. In sample 4611A, thin (>1mm) calcite veins, and a thicker (3-8mm) carbonate vein, cross-cut the matrix (Fig. 11b). The thicker vein appears to be cored by 1-2mm anhedral anhydrite crystals, rimmed by larger (up to 4mm) subhedral to euhedral calcite crystals (Fig. 11b).

Thin sections of the green and pink finely foliated gneiss are characterized by elongate polygonal quartz crystals, feldspar grains that exhibit weathered and/or perthitic textures, and fibrous and platy chlorite, biotite, and muscovite (Fig. 11c). These feldspar grains appear to account for the pink rimming along fracture boundaries, whereas the green and black groundmass is primarily composed of quartz, micas, and some olivine (Fig. 11c). Garnets are common, and are often brecciated.

The dolomitic groundmasses intermittently appear one meter below the contact and increase in density with depth. Dolomite primarily exists as a fine-grained, amorphous matrix and/or fine-grained veins (Fig. 11 d, e). The bottom 3 meters of the logged section are dominantly composed of this dolomitic groundmass, and are accompanied by a decrease in grainsize throughout the thin sections and spherulitic recrystallization textures in quartz grains (Fig. 11e).

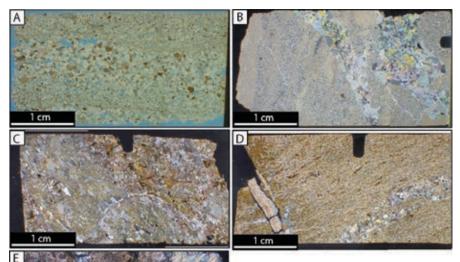


Fig. 10: Photomicrographs of thin sections from the CPC BD-139 core, representative of the 5 main lithologies captured the logged by section. (A) Sample 4607, graded bedding in the basal Mt. Simon Sandstone, with blue epoxy to highlight porosity. (B) Sample

4611A, dolomitized gneiss at the contact. The

large vein in the top right corner of the thin section is composed of anhydrite at the core, and calcite at the rim. (C) Sample 4613B-1, finely foliated green altered gneiss with sub-vertical pink-coated fractures. (D) Sample 4631.9, dolomitized gneiss at the base of the logged section. Metamorphic fabric is retained in the dolomite matrix. 1-2 mm thick quartz veins are cross-cut by a thicker (3 mm) fine-grained dolomite vein. (E) Sample 4633 under 5x magnification, spherulitic quartz in dolomitic groundmass

(left) with coarse-grained crystalline dolomite vein (right).

Mineralogical Analysis

X-ray diffraction (XRD) of 15 samples from the CPC BD-139 core (Table 1) reveals that the Mt. Simon Sandstone within a meter of the nonconformity primarily consists of quartz with minor nontronite-rich (iron-rich) clay. Quartz and feldspar make up the major phases of the gneissic basement host rock. The uppermost 30 cm of basement rock at the contact is depleted in quartz and feldspar relative to the host rock, and consists primarily of dolomite, with some minor sulfides (Table 1). Dolomite is a major mineral phase in 5 of the 14 analyses run on the basement rocks. Ankerite is also present in varying amounts. Clinochlore is present in trace amounts. Common alteration minerals include clays (primarily nontronite and vermiculite), phlogopite, and a variety of zeolites.

Table 1. Interpretation of XRD results for samples from the CPC BD-139 core. Green indicates a major mineral phase (PANalytical X'Pert Highscore score of 0.5 or higher), yellow indicates a minor mineral phase (score of 0.1-0.5), and orange indicates a trace mineral phase (score of <0.1). Abbreviations of mineral name is present where applicable.

ITHOLOGY	SAMPLE ID	/ 2	(B) B) COT	RILO	/	ar date	and of	part (Property	ANT CAN	
MT. SIMON	4608				nont.					
	4611A					dolo.			CuFeS2	
	46118								- Sell-Charles	
	4612			- 1				i i	9 1	
	4613A					dolo.			4 5	
	46138									
	4616.5								5	gism.
DACELIENT	4620A			9		ank., dolo.		FeAlphos.		
BASEMENT	4620B				verm.		The state of the s			
	4621		phl	ogo.	100		NaMnOx		AgAuS	
	4623		0	- 8		ank.				
	4625.5					-				
	4630.5				verm.	dolo.		clinochlore		
	4631.9			8		dolo.	NaMnOx		9	
	4633					dolo.		clinochlore		

Geochemical Analysis

Major and trace element whole rock analyses were run on 4 samples from the basement rocks in the CPC BD-139 core. The basement rocks at the contact (1405.43 m) are depleted in SiO₂ (36.16 wt%), with respect to unaltered gneiss (66.44 wt%). CaO and MgO are enriched at the contact (30.91 wt% CaO, 18.26 wt% MgO) and form a ~1 meter thick zone at the base of the logged section (1412.14 m, 21.40 wt% CaO, 19.45 wt% MgO) with respect to unaltered gneiss (0.3 wt% CaO, 5.58 wt% MgO). The unaltered gneiss is enriched in K₂O and Al₂O₃ relative to the rocks at the contact and at the base of the logged section. The contact rocks are depleted in FeO with respect to the rest of the core.

Barium, V, Cr, and Zr are the primary enriched trace elements constituents in the four analyzed samples. Barium is most concentrated in unaltered gneiss (1409.85 m, 894 ppm), and depleted at the base of the core (123 ppm). The unaltered gneiss is enriched with vanadium (309 ppm) and zirconium (313 ppm) with respect to the rest of the sampled core. The lowermost sample (1412.14 m) is highly enriched in chromium (2233 ppm) with respect to the rest of the sampled core.

Three calcite veins were identified in thin section and analyzed for oxygen stable isotope values in order to investigate possible source fluids of mineralization using oxygen thermometry. The $\delta^{18}O_{SMOW}$ values for the 3 veins range from 19.23 to 23.93% (Table 2).

Table 2: Oxygen stable isotope ratios for vein samples from the CPC BD-139 core. Calibrated data is precise to $\pm 0.01\%$.

Sample	description	δ ¹⁸ O‰ (SMOW)	δ ¹⁸ O‰ (VPDB)
CPC-4611A	calcite/anhydrite stringer vein	23.07	-7.60
CPC-4623	rimmed calcite vein	19.23	-11.33
CPC-4630.5	calcite vein perpendicular to fabric	23.93	-6.77

In the CPC BD-151 core (Fig. 12), the basal meter of the Mt. Simon Sandstone is a very tight, pinkish-tan sandstone with fine-scale laminae, possibly carbonate-cemented, with possible evidence for bioturbation or soft sediment deformation. This gives way to sub-

horizontally laminated gneiss that is especially weathered at the contact (~1434.39 m depth) (Fig. 12). The weathered gneiss at the contact is a 7-10 cm thick green gneiss. Below this lies about 3 meters of weathered pink and green gneiss with a granulite texture. A sub vertical alteration zone cross-cuts the older gneissic fabric at 1437.44 m depth. This lithology gives way to a hornblende-feldspar-quartz gneiss with 0.5-2 cm banding and horizontal to subhorizontal mineralized and partly mineralized fractures, which continues through the bottom of the logged section (Fig. 12).

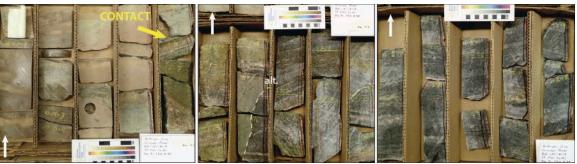
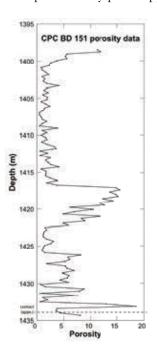


Fig. 11: Core photos of the CPC BD-151 core. The contact is at ~1434.39 meters depth, and is indicated by the yellow arrow. White arrows indicate up direction. Note sub-vertical alteration crosscutting gneissic fabric. Core is 7.6 cm in diameter.

Legacy data acquired by Maness Petroleum Laboratories and stored in well files at the Michigan repository provided brine injection step permeability tests for 2 depths, and porosity and permeability data for the CPC BD-151 core. Permeability and porosity data extends through the basal Mt. Simon Sandstone, truncating at the contact. Porosity in the sandstone fluctuates between 2-5%, with high (10-15%) porosity zones at 1400 and 1418 meters. Porosity increases to approximately 18% at the contact (1434 m), before dropping to approximately 4% directly below the contact. Data ends at 1435 meters (Fig. 13). In the provided dataset, permeability fluctuates between <10-17 to 10-13 m-2 permeability peaks appear to be more frequent above 1420 meters.



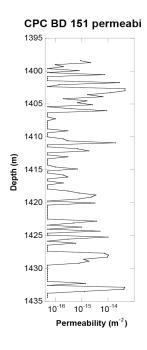


Fig. 13: A. Legacy porosity data for the CPC BD-151 core, gathered by Maness Petroleum Laboratories.

Porosity in the sandstone fluctuates between 2-5%, with higher (10-15%) zones at 1400 meters and 1418 meters. Porosity is highest at the contact (1434 meters). B Legacy permeability data for the CPC BD-151 core, gathered by Maness Petroleum Laboratories. Values consistently fluctuate between $<10^{-17}$ to 10^{-13} m⁻² throughout the 36 meters for which data were provided.

Step permeability tests were done at 1428.90 m and 1432.87 m, in the basal sedimentary rocks (Error! Reference source not found. 14), by injecting brine (1.21 g/cc, 0.6 pH, 2.244 cp) and 15% HCl (1.233 cp and 1.068 g/cc at 70° F). Both fluids were injected in 5 mL aliquots for each step. Permeability is highest in the shallower sandstone. Permeability stays fairly constant with brine injection at both depths, whereas acid injection causes an increase in permeability, particularly in the shallower test (Error! Reference source not found.14).

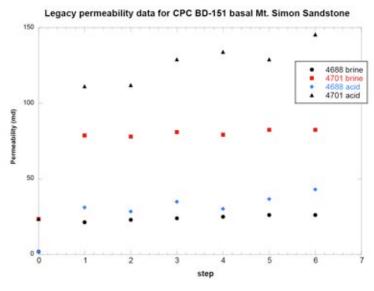


Fig. 14: Legacy step permeability tests for brine and acid injection into basal sedimentary rocks at two depths in the CPC BD-151 core, gathered by Maness Petroleum Laboratories. Permeability stays fairly constant with brine injection, and increases slightly with acid injection. Permeability for brine and acid injection is highest in the shallower sandstone.

UPH-1 Borehole

A total of 16 samples over a depth of 20.5 meters were obtained from the UPH-1 core. Sample numbers reflect the depth (in feet) at which samples were taken. The logged section of the UPH-1 core is comprised of 15 meters of Mt. Simon Sandstone and 7.9 meters of Precambrian granite (Error! Reference source not found.15). Five major lithologies were identified and described at the UPH-1 core in Mt. Horeb, Wisconsin (sandstone, siltstone, granitic wash, weathered basement, fresh basement). At this location the Mt. Simon Sandstone is tan and purple, cross-bedded, medium-grained, and well sorted, grading into an interbedded red and green siltstone at approximately 600 meters depth (Fig. 15). The interbedded siltstone is 5 meters thick, and grades over a short distance into an interbedded grus and siltstone layer (Error! Reference source not found.15). The interbedded grus layer is 2.8 meters thick, friable and clay-rich, contains sub-angular granite clasts (>1-3 cm in diameter), and is in sharp contact with Precambrian granite (Error! Reference source not found.15). The Precambrian granite is a pink, coarse-grained granite with no faults and few fractures (Fig. 15). Rare/minimal clay alteration of feldspar was identified at the contact (Fig. 15), and is absent with depth away from the contact.



Fig. 15: Core photos for the UPH-1 core from 593-616 m depth, in Mt. Horeb, Wisconsin. White arrows indicate up direction. White dashed line indicates location of contact (607.8 meters). Core is 3" in diameter.

A total of 7 thin sections from the UPH-1 core were analyzed. The two thin sections from the sandstone lithofacies of the Mt. Simon Sandstone reveal rounded to sub-rounded, well sorted, medium to coarse quartz grains cemented by quartz. Blue epoxy on these samples reveals a porosity of 8-12% (Fig. 16). One thin section of the siltstone lithofacies reveals sub-rounded to sub-angular, well sorted, very fine quartz cemented quartz grains, and a porosity of >3% (Fig. 16b). The grus horizon consists of gravel-sized, sub-angular to sub-rounded, quartz and clay-altered feldspar grains in a poorly sorted very fine to coarse-grained matrix with clay cement (Fig. 16c).

Thin sections of Precambrian granite reveal a coarse-grained alkali feldspar granite. Clay alteration of feldspar grains occurs at the contact, and appears to decrease with depth. Quartz and feldspar grains contain abundant microfractures, typically filled with clay, which are less abundant with depth over a range of ~5 meters (Fig. 16 d, e). Clay alteration of grains, interstitial clay, and clay-filled fractures are often accompanied by a relative increase in porosity.

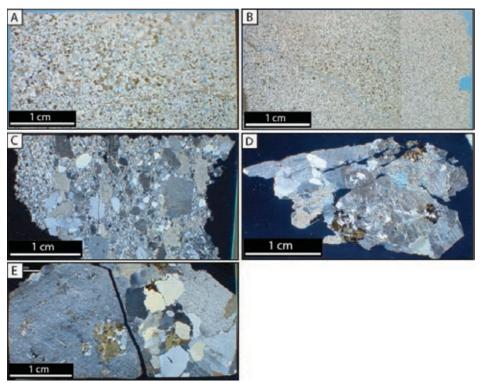


Fig. 16: Photomicrographs of thin sections from the UPH-1 core, representative of the 5 main lithologies captured by the logged section. (A) Sample 1962.4, representative Mt. Simon Sandstone. (B) Sample 1973.8, silty Mt. Simon Sandstone. (C) Sample 1994A, grus horizon directly at the contact containing interstitial clay and clay-altered feldspar grains. (D) Sample 1994B, clay-altered alkali granite directly at the contact. Note increase in porosity (blue patches) in altered feldspar grains and along microfractures, relative to surrounding host. (E) Sample 2013.2, representative unweathered alkali granite host rock, 5.8 meters below the contact.

The Mt. Simon Sandstone primarily consists of quartz with minor amounts of

feldspar and illite, and trace amounts of glauconite and iron oxide (

Table 3, Appendix C). Nontronite (the Fe-rich end member of the smectite clay mineral group) is a major mineral component within 6 meters above the contact. The basement rocks directly at the contact are primarily quartz and feldspar with trace palygorskite and ankerite. The slightly altered basement consists mainly of quartz, minor feldspar and nontronite, and traces of biotite. Unaltered host granite consists mainly of quartz and feldspar (albite, microcline, anorthite), with minor amounts of biotite and/or phlogopite (

Table 3).

Major and trace element whole rock analyses were run on 3 samples from the UPH-1 core, capturing the geochemical makeup of the unaltered sandstone, grus, and unaltered basement lithologies (Appendix D). The grus is depleted in SiO₂ with respect to the unaltered sandstone, and enriched in Al₂O₃ and K₂O with respect to the unaltered sandstone. The grus is slightly enriched in FeO with respect to the unaltered sandstone. The unaltered basement is primarily composed of SiO₂ (71.73 wt%), Al₂O₃ (14.07 wt%), and K₂O (7.00 wt%). The unaltered basement is also slightly enriched in Na₂O, FeO, and CaO relative to the grus and unaltered sandstone.

Table 3: Interpretation of XRD results for samples from the UPH-1 core. Green indicates a major mineral phase (PANalytical X'Pert Highscore score of 0.5 or higher), yellow indicates a minor mineral phase (score of 0.1-0.5), and orange indicates a trace mineral phase (score of <0.1). Abbreviations of mineral name is present where applicable.

LITHOLOGY	SAMPLE ID	iti keld	is part of	ays ri	igis garbi	mate [*] o ⁱ d	ě.
	1943.5						
	1945.5		illite				
	1946						
	1962.4						
MT. SIMON	1963.8		illite			Fe3O4	
IVII. SIIVION	1967			glauc.			
	1971						
	1971.5			musc.		rutile	
	1973.8		nont.			SrFeMoOx	
	1986.5		nont.	musc.			
	1994B		paly.		ank.		
DACENAENT	1997		nont.	bt			
BASEMENT	1998.5			bt			
	2013.2			phlogo.			

Zirconium, barium, strontium, and rubidium are the primary trace elements constituents in the three analyzed samples. The unaltered sandstone contains 1216 ppm zirconium. All other trace elements fall below 15 ppm. The grus sample is enriched in barium, zirconium,

rubidium, and strontium, and depleted in zirconium, with respect to the unaltered sandstone. The unaltered basement sample is enriched in barium relative to the grus and the unaltered sandstone. Unaltered basement is slightly enriched in rubidium, strontium, and zirconium, relative to the grus.

Marquette, Michigan

There are 3 outcrops that expose the nonconformity at the Marquette locality. At Hidden Beach, the nonconformity is exposed for less than a meter, and is overlain by 25 meters of the Neoproterozoic Jacobsville Sandstone. Other exposure was examined from sea kayak on Little Presque Isle and also reported in Hamblin (1958). Patches of exposed contact at Hidden Beach and on Little Presque Isle reveal that the basal Jacobsville Sandstone is interbedded with a cemented conglomerate consisting of sub-angular to rounded jasperoid, gneiss, and greenstone clasts (Fig. 17a). The overlying Jacobsville Sandstone contains vertical fractures with bleached horizons 15-90 cm wide (Fig. 17a,b). The bleached horizons are only in the Jacobsville Sandstone, and are associated with sub-vertical fractures and bedding planes. In some cases, fractures truncate at the basal conglomerate (Fig. 17a). Local relief on the nonconformity at Little Presque Isle is approximately 5-10 meters, and epidote-iron oxide coated faults and fractures roughly align with the bleached fracture zones in the Jacobsville Sandstone (Fig. 17a,c). The Compeau Creek Gneiss, with septa of the Mona Schist, underlies the Jacobsville at this site (Gair and Thaden, 1968b). Exposed surfaces appear fairly fresh due erosive processes occurring at the lake shore. Thin (>1-4 cm) linear veins consist of quartz, and in some cases, epidote. Small displacement (3-12cm) faults in the Compeau Creek Gneiss are epidote or quartz filled (Fig. 17a,d). No faults were observed in the Jacobsville Sandstone.



Fig. 17: Outcrop photos of Hidden Beach and Little Presque Isle, Marquette, Michigan. (A) The Jacobsville Sandstone basal conglomerate. Note sub-vertical bleach fracture truncating conglomerate layer. 15x18 cm field card for scale. (B) Bleached sub-vertical fractures in the Jacobsville Sandstone. Note person (1.68 m) for scale. (C) Epidote-iron oxide coated fault in the Compeau Creek Gneiss. These basementhosted faults often align with the overlying bleached vertical fractures in the Jacobsville Sandstone. Yellow ruler (10 cm) for scale. (D) Epidote-coated small displacement fault offsetting a quartz vein in the Compeau Creek Gneiss. Offset is ~1 cm.

The Presque Isle site provides ~1 kilometer of exposed nonconformity, though the overlying Jacobsville Sandstone is commonly eroded away due to lake shore processes. The contact is sinuous and has a topographic variation of ~2.5 meters over a span of 1100 meters (Fig. 18). The Jacobsville Sandstone here exhibits bleaching patterns that reflect zones of higher permeability (i.e. bedding planes, fractures) similar to that seen at Hidden Beach (Fig. 19a). Iron oxide and/or clay alteration of the Jacobsville Sandstone is common

(Fig. 19a,b). The basal Jacobsville Sandstone contains tight, cohesive conglomerates and friable, incohesive basal conglomerate units, primarily consisting of jasperoid clasts, with some quartz, feldspar, and sandstone clasts (Fig. 19a-c). The conglomerate exists as lenses and layers that vary laterally in thickness from 5 to 100 cm. Some conglomerate layers lie directly in contact with the serpentinized peridotite basement rock, whereas in other places, a layer of Jacobsville Sandstone lies between the conglomerate and serpentinized peridotite (Fig. 19a,b, c). In some areas a regolith horizon up to 1 meter thick exists at the top of the basement (Fig. 19a,d). The serpentinized peridotite basement rocks at this site range from black to red, with white web-like stockwork vein patterns (Fig. 19a,e,f). Jasperoid veins are up to 10 cm thick (Fig. 19a,f). The texture of the serpentinized peridotite ranges from crumbly and incompetent to moderately cohesive rock. Near-vertical fractures often exist in both the Jacobsville Sandstone and the serpentinized peridotite, although fracture density is often lower in the serpentinized peridotite, fractures in the Jacobsville sandstone truncate at the basal conglomerate layer or at the contact (Fig. 20). The various geometric relationships between the Jacobsville Sandstone, conglomerate unit(s), regolith, basement rock, faults, and fractures, are documented through a series of lithologic columns in Fig. 20. Normal, oblique, and strike-slip faults at Presque Isle are primarily basement-hosted. In some areas that captured a full vertical section through the contact we observed basement-hosted normal and oblique faults truncating at the contact, and a normal fault bisecting the contact (Fig. 21). Three of the four faults observed at Presque Isle are associated with iron-oxide mineralization. The one faulted site that did not contain significant iron-oxide mineralization bisects the contact and basal conglomerate, appearing as a silica-rich vein with a lozenge-like structure in the basement, on which slip surfaces were observed. This vein pinches out into the basal conglomerate, extending as an unmineralized, planar fault surface through the conglomerate? (Fig. 21a). Slip surfaces on 4 faults observed at Presque Isle range in thickness from (<1-15mm).

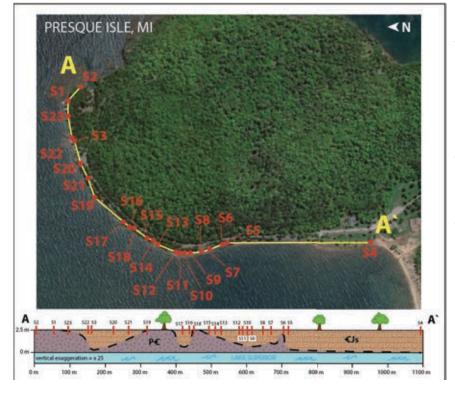


Fig. 18: Topographic variation of the contact at Presque Isle was mapped using lithostratigraphic profiles measured at each station (location of station indicated by red vertical line). The nonconformity along the ENE shore of Presque Isle varies vertically by 2.5 meters over a distance of 1100 meters.

Four thin sections from the Hidden Beach site and 17 thin sections from the Presque Isle site were analyzed. The Jacobsville Sandstone consists of fine-grained, angular, moderately sorted quartz and feldspar grains. A thin section capturing the transition from red sandstone protolith to a bleached horizon adjacent to a fracture at Hidden Beach reveals little change in texture and composition, and a reduction in hematite grain coatings and cement from the red to the bleached sandstone (Fig. 22a).

Incohesive and poorly cemented onglomerates consist of rounded gravel- to small pebble-sized clasts of quartz and feldspar cemented by clay, hematite, and calcite (Fig. 22b). Clasts are often rimmed by void-space, and some clasts appear altered (Fig. 22b). Calcite cement is either sparry or amorphous (Fig. 22c). Thin sections of the mineralized, competent conglomerate reveal little porosity, and dominantly consist of chalcedony in a fine-grained, poorly sorted, angular quartz grains in hematite cement. Clasts of the serpentinized peridotite basement host rock are rare. (Fig. 22d).

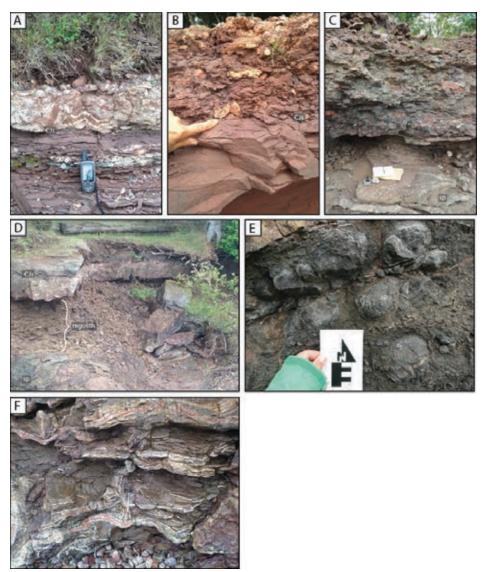


Fig. 19: Outcrop photos of nonconformity exposures at Presque Isle, Marquette, Michigan. (A) Mineralized conglomerate in the Jacobsville Sandstone primarily consisting of jasperoid clasts. Note reduction along bedding planes. GPS (6x16 cm) for scale. (B) Significant iron oxide mineralization in the Jacobsville Sandstone and basal conglomerate unit. Hand for scale. (C) The basal conglomerate

unit in the Jacobsville Sandstone lying directly in contact with serpentinized peridotite basement rocks. Compass (8x8 cm) for scale. (D) Regolith horizon (~80 cm thick) above the serpentinized peridotite at the contact. (E) Spheroidal weathering pattern in the serpentinized peridotite. Field card (15x8 cm) for scale. (F) Stockwork veining patterns and thick (<10cm) jasperoid veins in the serpentinized peridotite. Pen (15 cm) for scale.

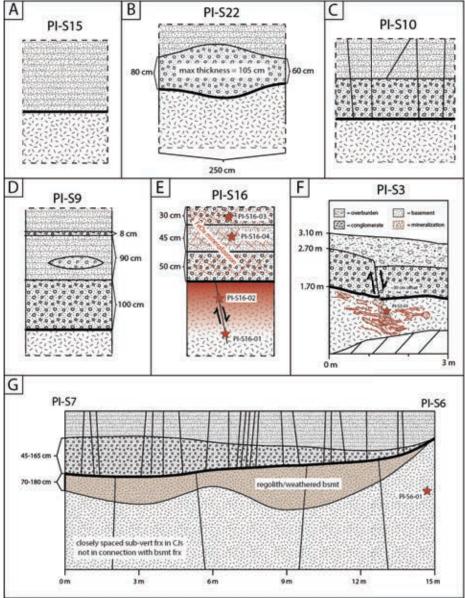


Fig. 20: Litho-stratigraphic columns constructed from nonconformity exposures at Presque Isle, Marquette, Michigan. (A) Sharp contact between The Jacobsville Sandstone and serpentinized peridotite, faults and conglomerate absent. (B) Conglomerate horizon of varying thicknesses in contact with serpentinized peridotite, faults absent. (C) Conglomerate horizon in contact with serpentinized peridotite, fractures in the Jacobsville Sandstone truncating at basement, and at the conglomerate. (D) Variable distribution of conglomerate horizon in the Jacobsville Sandstone, including lenses and layers of variable thickness. (E) Fe-mineralization is concentrated in the Jacobsville Sandstone, and decreases with depth from the contact in the basement. Red stars indicate sample locations. Normal fault truncates at the contact. (F) Normal fault bisecting the contact. Fault appears as a silica-rich vein with a lozenge-like structure in the basement rocks. (G) Regolith at the

top of the basement and basal conglomerate laterally pinching out. Fractures exist in the Jacobsville Sandstone and the basement, and are not in connection.

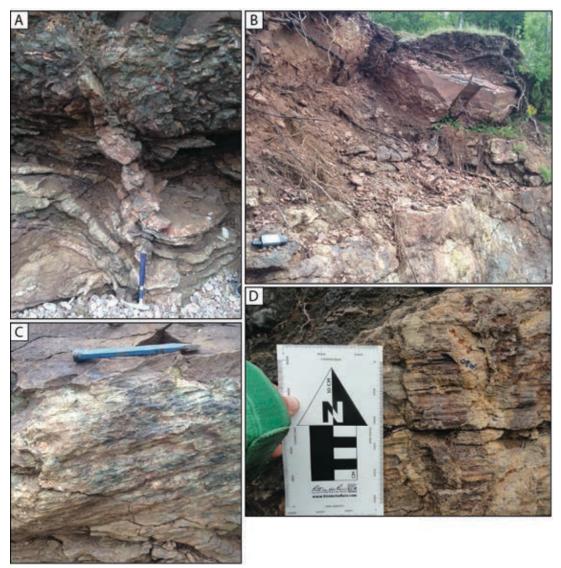


Fig. 21: Field photographs of basement-hosted faults at Presque Isle, Marquette, Michigan. (A) Normal fault bisecting the contact and the basal conglomerate in the Jacobsville Sandstone. This fault presents itself as a silica-rich vein with a lozenge-like structure in the basement, which partially extend up into the offset mineralized conglomerate layer. Rock hammer (28 cm tall) for scale. (B) Dip-slip fault surface truncating at the contact. GPS (6x15 cm) for scale. (C) Oblique fault slip surface in serpentinized peridotite. Chisel (15 cm) for scale. (D) Mineralized strike-slip fault surface in darker, relatively less competent serpentinized peridotite. Tan mineralization is 1-1.5cm thick. Field card (15x8 cm) for scale.

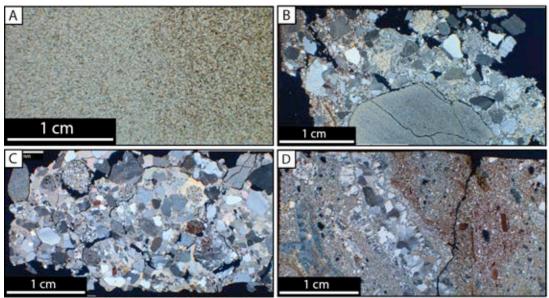


Fig. 22: Photomicrographs of thin sections of the Jacobsville Sandstone and basal conglomerate, from Hidden Beach and Presque Isle, Marquette, Michigan. (A) Sample WET-5, transition between the bleached Jacobsville Sandstone (left) and the unbleached Jacobsville Sandstone host (right). (B) Sample WET-A, incohesive basal conglomerate. Note thin void space surrounding large clast, and slight alteration around rim of large clast. (C) Sample HB-S4-01, sparry calcite-cemented conglomerate. (D) Sample PI-S5-04, cohesive, fine-grained conglomerate consisting of quartz grains and Jacobsville Sandstone pebbles.

Thin sections of the serpentinized peridotite from Presque Isle host reveal variable lithology of the basement rocks. Altered, incohesive serpentinized peridotite samples consist of thin, stringy stockwork-textured dolomite veins in a matrix of relatively high (3-5%) porosity hematite-replaced serpentine, with small amounts of magnetite (Fig. 23a). The more basement lithology consists mainly of patchy dolomite and recrystallized quartz with some hematite and magnetite. Veins are thin (>1-2 mm) and consist of fine-grained dolomite (Fig. 23b). Basement-hosted veins consist of both silica and calcite or dolomite. Silica veins are characterized by recrystallized amorphous quartz crystals or fibrous chalcedony crystals oriented perpendicular to vein boundaries. Calcite or dolomite veins cut silica veins (Fig. 27c). Calcite veins hosted in intact serpentine basement protolith exhibit syntaxial fibrous texture similar to the textures observed in calcite beef (Cobbold et al., 2013). Fibrous vein textures are also incorporated into crack-seal vein textures (Fig. 23d).

Six types of basement-hosted slip surfaces from the Presque Isle serpentinized peridotite are seen in thin section (Fig. 24). No slip surfaces from Hidden Beach were observed in thin section. Calcite slip surfaces typically 2-20 cm thick are common. Crystal texture ranges from coarse massive aggregates to fibrous crystals oriented perpendicular to slip. Shear along the slip surface is not apparent. Some calcite-rich slip surfaces contain fibrous serpentine, and show a relative increase in porosity (Fig. 24a-c). Slip surfaces may also be composed of clay and radiating chalcedony oriented perpendicular to slip (Fig. 24d,e). The Jacobsville Sandstone is primarily composed of quartz and nontronite and trace amounts of hematite, rutile, vermiculite, zeolites, and clinochlore (Table 4). The conglomeritic basement layer consists mainly of quartz and nontronite, with trace zeolites and iron oxide. Mineralogy of the serpentinized peridotite protolith is variable. Dolomite, serpentine, quartz, iron oxide, and talc, are present in varying amounts. Dolomite and quartz are the most common major mineral phases. Lizardite, antigorite, chrysotile, iron oxide, and talc are generally minor phases. Veins within the basement rock consist of quartz, serpentine, dolomite, sepiolite, and

talc. Slip surfaces are dominantly comprised of quartz with minor dolomite and trace oxides (Table 4).

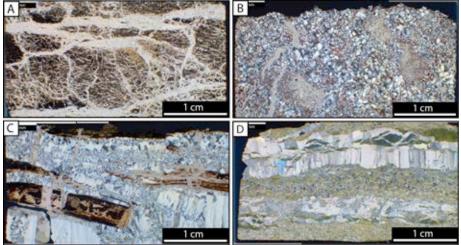


Fig. 23: Photomicrographs of serpentinized peridotite host rock and veins from Presque Isle, Marquette, Michigan. (A) Sample PI-4, stockwork- to mesh-vein textures are observed in incohesive serpentinized peridotite. Veins are composed of dolomite, and host is highly altered and Fe-rich. (B) Sample PI-S5-01, cohesive, mineralized, serpentinized peridotite. Matrix is dominantly patchy finegrained amorphous dolomite, iron oxide, and recrystallized quartz. Fine-grained dolomite veins cross-cut the matrix. (C) Sample PI-vein, chalcedony, dolomite, and calcite veins in serpentinized peridotite host. Calcite veins are oriented perpendicular to, and offset by, dolomite and chalcedony veins. (D) Sample CG-host, crack-seal and fibrous beef-like calcite veins in a relatively unaltered serpentinized peridotite host.

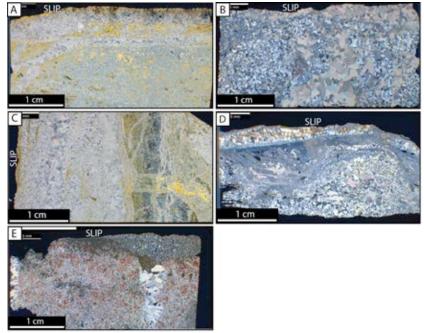


Fig. 24: Photomicrographs of basement-hosted slip surfaces from Presque Isle, Marquette, Michigan. Location of slip surface is marked by word 'SLIP' in white for each microphotograph. (A) Sample PI-S2-02, calciterich surface slip dolomitized serpentinized peridotite. (B) Sample PI-S16-02, crystalline calcite slip surface in quartz-rich mineralized serpentinized peridotite. (C) Sample PI-S2-01a, thick calcite slip surface

anastomosing geometry in serpentinized peridotite. (D) Sample PI-S16-01, chalcedony slip surface in dolomitized serpentinized peridotite. The host rock directly beneath the slip surface is relatively porous. (E) Sample PI-S3-01, fine-grained quartz slip surface in relatively porous, Fe-rich serpentinized peridotite host. The slip surface cross-cuts a coarse-grained quartz vein.

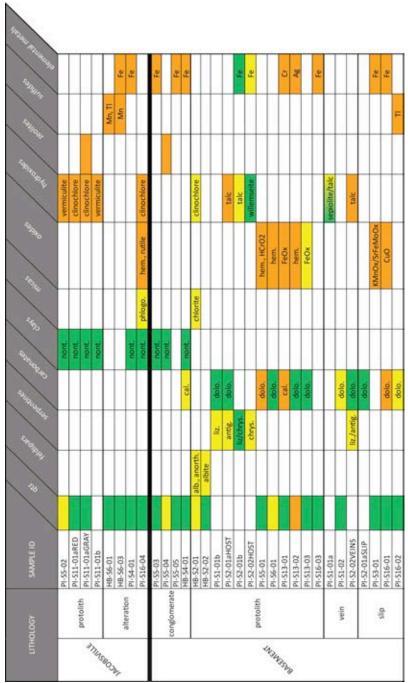


Table 4: Interpretation of XRD results for samples Hidden Beach and Presque Isle, Marquette, MI. Green indicates a major mineral phase (PANalytical X'Pert Highscore score of 0.5 or higher), yellow indicates a minor mineral phase (score of 0.1-0.5), and orange indicates a trace mineral phase (score of <0.1). Abbreviations of mineral name is present where applicable.

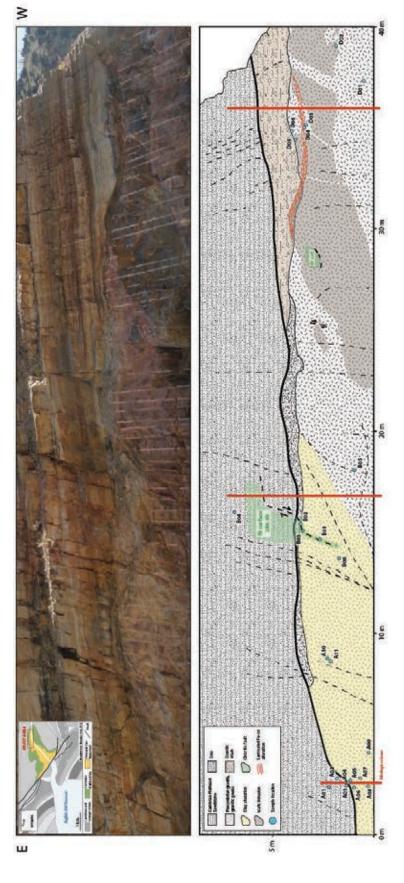
Cody, Wyoming

The Cambrian Flathead Sandstone and Precambrian granite contact west of Cody, Wyoming provides access to 40 meters of the nonconformity, adjacent exposures of the basal Flathead Sandstone, the uppermost section of basement rock, and a small fault that cuts the section. An east-west trending map-scale fault that cuts the rocks, and may tip out at the outcrop study site (Fig. 25).



Fig. 25: Map-scale fault in Cody, Wyoming. The orientation of the main outcrop (circled in yellow) at the Cody, Wyoming locality is roughly parallel to that of a probable fault (red). Slip on roughly E-W oriented surfaces at the main outcrop and secondary observation sites, and remote observations of probably fault gouge, indicate the presence of an E-W striking map-scale fault.

The sinuous 40 meters map distance contact exposed at the Cody locality and alteration along the contact varies laterally (Fig. 26). Alteration of basement rocks is apparent at the eastern end of the exposure, decreasing to the west (Fig. 26). The eastern 25 meters of the contact consists of a >5-50 cm thick weathered horizon at the top of the basement. The western 15 meters of the contact is underlain by a layer of horizontally laminated 'granitic wash', consisting of mostly clay and sub-rounded gravel-sized clasts of granite. The granitic wash is fairly unconsolidated in the bottom 85 cm, whereas the top 85 cm is cemented (Fig. 27a,b). A sinuous, ~30 cm thick, laminated iron oxide horizon lies below the horizontally laminated granitic wash horizon, possibly related to the mafic intrusive rocks in this portion of the exposure (Fig. 27c). Near-vertical fractures bisect the contact, and sandstone- and basement-hosted fractures truncate at the contact. Small faults occur in both crystalline basement and sedimentary rocks. Sedimentary-hosted faults exhibit quartz, clay, and hematite mineralization on slip surfaces. Basement-hosted faults are typically quartz- or clay-rich, or chloritic. Faults are primarily roughly E-W oriented. One fault was found to bisect the contact (Fig. 28).



Precambrian granite and granitic gneiss is exposed in a road cut approximately 9 km west of Cody, Wyoming, in the shallow east-dipping limb of Rattlesnake Mountain. The Flathead Sandstone exhibits little alteration. Alteration is concentrated in the basement rocks along the contact, varying laterally in degree, type, and thickness. A clay alteration horizon (yellow) in the granitic basement rocks extends up to 2 meters or more below the Fig. 26: Field photograph and annotated tracing of the main outcrop in Cody, Wyoming. The contact between the Cambrian Flathead Sandstone and contact in the eastern portion of the outcrop, and is sparse to absent in the western half of the outcrop. A cohesive, finely laminated 'granitic wash' horizon (tan) consisting of sub-rounded feldspar clasts in a clay-rich matrix lies directly below the contact in the western 15 meters of the outcrop. A sub-horizontal, Fe-rich, laminated alteration horizon (red streaks) cross cuts to granitic wash and uppermost portion of the basement. Fault surfaces are commonly chloritic, Fe-rich, or clay-rich.

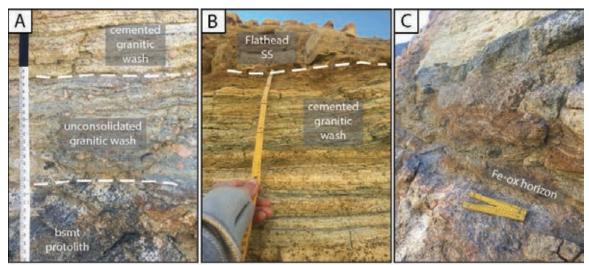


Fig. 27: Field photographs from the granitic wash horizon in Cody, Wyoming. (A) Cemented and uncemented granitic wash above mafic basement protolith. (B) Upper portion of cemented granitic wash, in contact with the Flathead Sandstone. (C) Laminated iron-oxide alteration horizon in mafic basement protolith below granitic wash horizon.

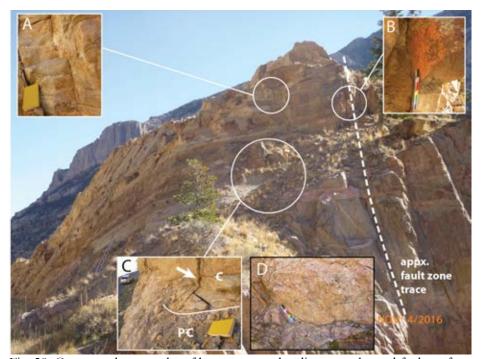


Fig. 28: Outcrop photographs of basement- and sedimentary-hosted fault surfaces at the western end of the main outcrop in Cody, Wyoming. The approximate trace of the E-W oriented fault zone is indicated by the white dashed line. Faults pictured in A-D are oriented roughly along strike. Sandstone-hosted faults (A,B) contain quartz, clay, and hematite. (C) Fault (indicated by white arrow) likely bisecting contact. (D) Example of basement-hosted fault (photograph location not in this image).

Thin sections from the Flathead Sandstone reveal an annealed quartz arenite with fine to coarse, poorly sorted, rounded to sub-rounded grains. Pore-spaces are typically filled with

iron-oxide (Fig. 29a). The sandstone in the deformation bands appear as silt-sized to very fine, poorly sorted, angular grains. Undeformed sandstone has an estimated porosity of around 13%, significantly decreasing within the deformation bands to <5% (Fig. 29b). Thin sections capturing the unconsolidated granitic wash layer at the contact reveal brecciated angular quartz and feldspar grains within a very fine brecciated quartz, feldspar, clay, and iron oxide matrix (Fig. 29c). One thin section capturing the cemented granitic wash layer reveals moderated sorted, medium-grained, rounded quartz cemented by calcite and possibly clay. Spots of iron oxide appear to form around large pore spaces (Fig. 29d).

Thin sections of pink granite protolith reveal a coarse-grained alkali granite with few muscovite lathes (Fig. 29e). A ~3-6mm thick mineralized fracture surface in the alkali granite consists of clay-sized to very fine grains of angular quartz and feldspar (Fig. 29f). Thin sections of slip surfaces in the alkali granite reveal a protolith with clay-altered feldspar. Slip surfaces are unmineralized, and are characterized as relatively finer-grained brecciated host rock (Fig. 29g). Crack-seal calcite veins from the mafic intrusive basement rock show evidence for multiple phases of fluid flow and fluctuations in fluid pressures (Ramsay, 1980). Textures within the crack-seal veins include brecciated calcite grains, sheared fibrous calcite grains (similar to calcite-beef texture), and dogtooth calcite grains (Fig. 29h).

Unaltered Flathead Sandstone is primarily composed of quartz, and in some cases, contains trace amounts of kaolinite and iron oxide. Altered Flathead Sandstone is dominantly composed of quartz, with traces of feldspar, kaolinite, phlogopite, ankerite, and iron oxide (Table 5). Mineralization in the form of deformation bands, as well as slip surfaces in the sandstone, are both dominantly composed of quartz, and sometimes trace amounts iron oxide. Unaltered pink granite is dominantly composed of quartz and feldspar, with trace kaolinite. The unaltered mafic intrusion is dominantly composed of quartz, with minor biotite, phlogopite, and gismondine (zeolite). The pink granite typically alters to clays (illite, kaolinite, nontronite, and dickite), and phlogopite becomes a more common minor constituent. Very altered granite samples are depleted in quartz and feldspar, and consist primarily of clay minerals. Calcite is found in trace amounts in 3 out of 10 altered basement host samples (Table 5). Altered mafic intrusive rock primarily consists of quartz, with trace clays (dickite, palygorskite, halloysite) and iron oxide. Mineralization in the pink granite consists mainly of quartz, with minor clays (dickite, kaolinite) and feldspar. Mineralization in the mafic intrusive rock is calcite-rich with minor quartz. Fault surfaces are quartz dominated, with minor amounts of feldspar, mica, trace, palygorskite and dickite (Table 5). Major and trace element whole rock analyses were run on 7 samples from the Cody, WY locality. Samples include unaltered Flathead Sandstone, a sandstone-hosted slip surface, cemented and un-cemented granitic wash, altered basement at the contact, and basement hosted slip surfaces. The geochemical makeup of the Flathead Sandstone and the sandstone hosted slip surface are dominantly composed of SiO₂ (>90 wt%). Al₂O₃ is enriched in the sandstone hosted slip surface (5.79 wt%) relative to the Flathead Sandstone host (2.48 wt%). All other major oxide constituents for the Flathead Sandstone and sandstone hosted slip are >1 w%. The granitic wash samples are dominantly composed of SiO₂ (77.0-89.9 wt%) and Al₂O₃ (3.09-10.53 wt%). The unconsolidated granitic wash (CWY-D03) is more enriched in Al₂O₃, than the cemented granitic wash (CWY-E01). Both granitic wash samples contain between 1.14-3.66 wt% FeO, 1.04-2.95 wt% K₂O, and 3.90-4.26 wt% CaO. The altered basement sample from the contact is enriched in SiO₂ (79.0 wt%) and Al₂O₃ (16.6 wt%). K₂O composes 2.58 wt% of the altered basement. All other major oxide constituents are >1 wt%. Basement hosted slip surfaces are mainly composed of SiO₂ (75.0-77.7 wt%), Al₂O₃ (13-41-14.84 wt%), and K₂O (4.94-8.16 wt%). One slip surface contains 3.78 wt% Na₂O. The remaining major oxide constituents for basement hosted slip surfaces are <1 wt%.

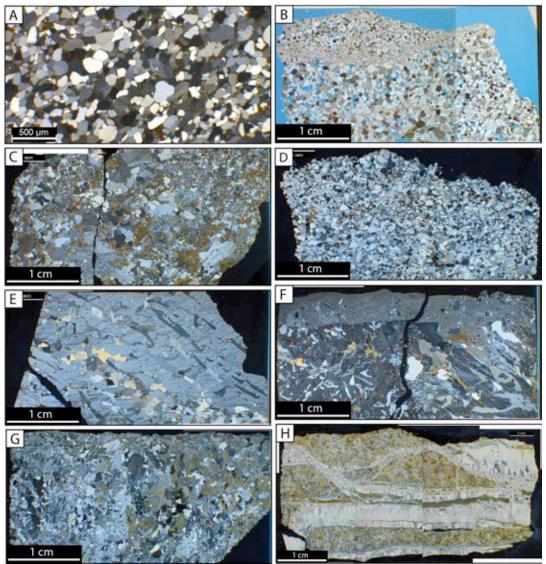


Fig. 29: Photomicrographs of samples from Cody, Wyoming. (A) Sample CWY-A01, Flathead Sandstone with hematite and/or iron-rich clay filling pore spaces. (B) Sample CWY-E06, variation in porosity in the Flathead Sandstone due to reduction of grain size in deformation bands. (C) Sample CWY-A03, grus layer from eastern portion of the main outcrop, consisting of angular, brecciated quartz and feldspar grains in a clay-rich matrix. (D) Sample CWY-E01, cemented granitic wash from the western portion of the main outcrop, primarily consisting of calcite-cemented quartz grains, and hematite-filled pore spaces. (E) Sample CWY-A10, unaltered alkali granite. (F) Mineralized fracture surface (top, 4-6 mm thick) in unaltered alkali granite, consisting of brecciated host rock in a matrix of clay and clay-sized quartz grains. (G) Slip surface in alkali granite (top). Slip surfaces are characterized by brecciation of host rock and a decrease in grain size along the surface. (H) Sheared fibrous calcite veins in mafic intrusive basement rock. Veins are 1-8 mm thick and often exhibit a crack-seal texture.

The dominant trace element constituents at the Cody locality are barium, zirconium, strontium, and rubidium. The sandstone hosted slip surface is depleted in zirconium relative to the sandstone host, but contains slightly more barium, strontium, and rubidium, as well as 138 ppm cesium. The unconsolidated granitic wash sample (CWY-D03) contains 1242 ppm barium, whereas the cemented granitic wash sample (CWY-E01) contains 79 ppm. The

altered basement sample at the contact is mainly enriched in strontium (163 ppm) and barium (364 ppm). One basement hosted slip surface (CWY-B03) is highly enriched in barium (2790 ppm) and slightly enriched in strontium and rubidium (119 and 116 ppm, respectively). The other basement hosted slip surface (CWY-D07) is relatively depleted in all trace elements (>170 ppm for each trace element).

Table 5: Interpretation of XRD results for samples from Cody, Wyoming. Green indicates a major mineral phase (PANalytical X'Pert Highscore score of 0.5 or higher), yellow indicates a minor mineral phase (score of 0.1-0.5), and orange indicates a trace mineral phase (score of <0.1). Abbreviations of mineral name is present where applicable. Gray shading on sample ID cells indicates mafic basement.

LITHOLOGY	Y 3	SAMPLE ID	/	1/1	1 1	10	/	8 / 3	, ol. oh	şuffd
		A01			kaol				Fe	/
he	pst	A02 :			1				Fe	
	- 1	£05b			There !					
4	and a	A03		1,100	kaol		ank		- Can	
ate miner	ered	A04		580.	kaol	phlog.	ank	-	Fe	
f miner	alized	E06		75.51						
		804								
- 8	100	E04							Fe	
25	Saft Safter	£05a								
(a)		E07								
-		AOE			kaol					
100	oue	A09host			Control Control					
. No	ost	A10				F-72		2.0		
		D02				bt, phlog		gismondine		
		A05			Ilite, dickite			1		
	- [A06			litte / kaol, dickite				Fe	
	- 1	A07			none	phlog				
	Ī	All			nont / dickite	PNUSE				
	ered	806								
- 400	erea	D03			nont	phlog	calcite			
13.90		D04			kaol, dickite	phlog			-	
		D05			dickite, palyg, halloy	120116		-	Fe	
48		E01			nont		calcibe		1000	
	_	E03			-		calcite			
	- 1	A09surf			kaol, dickite			1		
miner	ralized	F01			ilite / kaol				rutile	
		Q1					calcite		birminisite	
		A12	to 0	-	2			1 7	- Fe	
Made Market		801								tin sulfide
	1	802			palygorskite					
	1	803			La Tarchicologica				rutile	
198	0.00	D07			CHARLES P	phlog				
10-05-0	1	008	4		dickite	bt			CaCuPtiStiTeCl-ox	
	F03				MUNE		1	100000000000000000000000000000000000000		

Conceptual Models of Contact Types and Mineralization

We identify three categories of hydrologically significant nonconformity types in this study. These are: 1) basal conglomerate, 2) weathered and/or altered horizon (i.e., regolith, grus, granitic wash), and 3) mineralized contacts. Regolith refers to horizon of bedrock which has been weathered by surface processes, with little or no evidence of transport (Pain, 1991). Grus is a type of regolith in which the source rock is a felsic crystalline rock, resulting in a clay-rich material (Migon and Thomas, 2002). Granitic wash is a weathered material which is compositionally equivalent to the source rock, however, evidence of transport is present (Pettijohn et al., 2012). We stress that the three major contact type categories do not completely encapsulate the full range of geological scenarios that may be found at the nonconformity zone, but are a sampling of what one could expect to find at the nonconformity zone (Error! Reference source not found.) based on what we document from our five case studies.

Here we examine the geologic properties of each contact type from a hydrological prospective to hypothesize how the specific properties of each contact type pertain to fluid transport along the nonconformity. We predict the geologic features discussed below to be either conduits (permeability high relative to surrounding rock) or barriers (permeability low relative to surrounding rock), based on the geologic properties they display.

The permeability of the contact zone relative to the surrounding rock has significant influence on the propagation of fluid pressure (Zhang et al., 2013). The presence of a low-

permeability barrier at the nonconformity decreases fluid pressure propagation, therefore decreasing risk for injection-induced seismicity (Fig. 30) (Zhang et al., 2013; 2016; Ortiz, 2017).

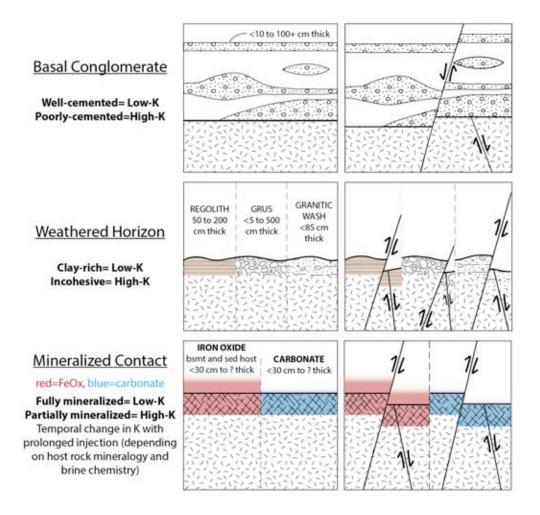


Fig. 30: Overview of the 3 main contact types and associated permeability. Low permeability horizons are likely associated with low seismic risk with injection, according to Zhang et al., (2013) and Ortiz, (2017). Faulting may be basement-hosted, or offset the contact. Drawings are not to scale

Basal Conglomerate Contacts

The presence of a basal conglomerate at the contact is observed in the Jacobsville Sandstone at Hidden Beach and Presque Isle, Michigan. Texturally, the basal conglomerate falls into two hydrologically distinct categories: 1) tight, well-cemented layer, which would likely act as a low permeability barrier to flow, and 2) friable, poorly cemented horizon, which may act as a conduit to flow (Figs. 30, 31). Thin sections of the two differing conglomerates reveal porosity in both samples. Porosity in the tight conglomerate is vuggy and disconnected (Fig. 31a), whereas the friable conglomerate has effective porosity in the form of fractures and void spaces along clast boundaries Fig. 31b). Geochemically, the tight conglomerate is more clay-rich relative to the friable conglomerate, further indicating that it may act as a low-permeability barrier to fluid flow (Table 4). The tight conglomerate type appears to be more common than the friable variety at the Marquette, Michigan sites, however, this may not

hold true elsewhere. The basal conglomerate at the Marquette, Michigan sites is spatially and geometrically variable. The basal conglomerate exhibits variations in lateral thickness, ranging from <10-100 cm. Conglomerate layers form lenses, are interbedded with the host sedimentary unit, and often pinch out. The basal conglomerate lies in contact with basement rock in some places, or is, in some places, absent all together (Fig. 32).

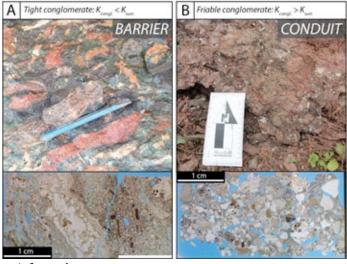


Fig. 31: Barrier- versus conduit-type basal conglomerate layers.

Tight, (A) well-cemented conglomerate layer at Presque Isle, Michigan. Marquette, Ineffective porosity is present in this type of conglomerate, and therefore likely has a low permeability (K) relative to the surrounding rocks. Chisel (15 cm) for scale. (B), poorly-cemented conglomerate at Hidden Beach, Michigan. Marquette, porosity interconnected this conglomerate type indicates that it may have a high K, relative to the surrounding rocks. Field card (8x15

cm) for scale.

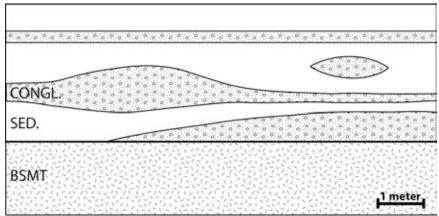


Fig. 12: Schematic diagram depicting the range of basal conglomerate geometries observed at Presque Isle, Marquette, Michigan. Geometries include lateral changes in thickness (pinch-outs, bulges, lenses) and direct and indirect contact with underlying basement rocks. In addition to the scenarios depicted here, the basal conglomerate may be completely absent in places.

Weathered and/or Altered Horizon Contacts

We observe three different types of weathered horizons at the contact at three different localities. Weathered horizons likely contain some degree of alteration, such as alteration of feldspars to clay minerals. The process by which these alteration minerals are formed differentiates this contact type from the 'mineralized' contact type, in which chemical alteration of the host rock is due to fluid-rock interaction as externally sourced fluids move along the contact, rather than from in situ surface weathering processes. The geochemistry of alteration minerals in weathered profiles resembles that of the host rock, whereas a mineralized horizon may be enriched in elements not found in the host rock. Additionally, textures revealed in thin section, such as sericitization of feldspar grains, can also be used to

distinguish between weathering-related chemical alteration and mineralization. At Presque Isle, some sites exhibit a regolith horizon at the top of the serpentinized peridotite, in contact with the overlying Jacobsville Sandstone (Fig. 33). This regolith horizon is between 50 and 200 cm thick, and is characterized as a very friable, unconsolidated, fine-grained material, which generally retains the color and texture of the underlying host rock (Fig. 33a). Dolomite- and silica-rich veins seen in the host rock are often preserved in the overlying regolith. In places the regolith horizon has completely weathered away, leaving a gap between the basement rock and overlying strata (Fig. 33b). The hydrological implications of a regolith horizon at the contact is highly dependent on the host rock from which it formed, but in the case of the Presque Isle regolith, we predict that it may act as a conduit to flow based on the highly incohesive texture and tendency to weather easily.

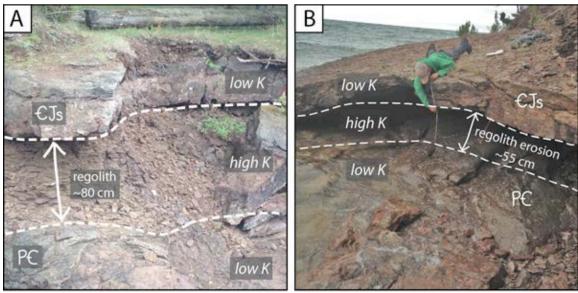


Fig. 33: Regolith horizons at the contact at Presque Isle, Marquette, Michigan. Relative permeability (K) of layers are indicated. (A) Regolith is significantly less competent than surrounding rock. (B) The friable nature of the Presque Isle regolith makes it particularly susceptible to weathering. Here the regolith has been eroded away by wave action on the lakeshore, leaving a gap between the underlying basement host rock and the overlying Jacobsville Sandstone mineralized basal conglomerate.

A grus horizon lies directly at the contact in parts of the Cody, Wyoming outcrop (Fig. 33). This weathered horizon is defined as grus rather than regolith or granitic wash based on the felsic parent rock, lack of evidence of transport, and relative clay content. The <5-30 cm thick grus horizon is characterized by sub-angular gravel- to pebble-sized granite clasts in a very friable, clay-rich matrix. Iron-oxide mineralization along a fracture boundary that bisects the grus horizon and adjacent lithologies is evidence of the movement of oxidizing fluids along a fracture plane (Error! Reference source not found. 33).

Granitic wash is observed at the Cody, Wyoming outcrop and in the UPH-1 core (Figs. 33, 34). In the UPH-1 core, the interbedded nature of the grus-like material is indicative of transport of a once in-situ weathered material, thus we define it as a granitic wash. The 2.8-meter-thick interbedded granitic wash layer is characterized as a relatively incohesive, clayrich material, containing sub-angular pebble-sized granite clasts (Fig. 34a). The granitic wash horizons in Cody, Wyoming are laminated and contain sub-rounded to rounded granite clasts, indicating transport. This granitic wash is very similar to the clay matrix-rich granitic wash seen in the UPH-1 core, with the main physical difference being that the granitic wash in Cody is laminated and contains clasts that are more rounded (Fig. 33, 34b). The high clay

content of the Cody granitic wash indicates that it may acts as a low-permeability barrier to fluid flow. In addition, the laminations in this material may result in anisotropic fluid

migration, relative to an unlaminated material (Fig. 35).



Fig. 34: Grus at the contact at Cody, Wyoming. Iron-oxide staining along the fracture boundary in the grus layer may be indicative of oxidizing fluid movement through fractured zones. Field card (15x8 cm) for scale.

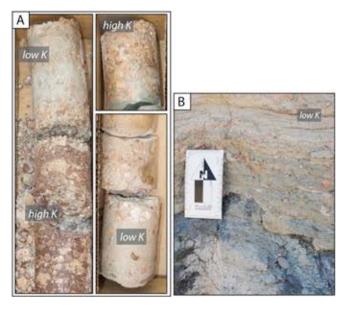


Fig. 35: (A) Granitic wash in the UPH-1 core. Relatively less clay-rich, clastsupported granitic wash is accompanied by iron oxide alteration, whereas the more clay-rich, matrix supported material is not. This may be indicative of microvariations in permeability due to differences in the clast to matrix ratio of the material. (B) Laminated, clay-rich granitic wash in Cody, WY. This material likely has a low permeability due to high clay content, relative to surrounding rock. Laminations would likely cause this material to behave anisotropically.

A weathered horizon was not observed in the CPC cores. Easton and Carter (1995) document a weathered contact zone in core from southwestern Ontario, which also samples the Grenville Front Tectonic Zone. The cores they documented contain a 2- to 5-meterthick zone of weathering and alteration at the contact in the uppermost basement rocks, at the contact between Cambrian sandstone and Precambrian granitic gneiss. They describe this as a 'paleo-regolith' which is primarily characterized by saussuritization of plagioclase, development of authigenic K-feldspar, and corrosion and chloritization of mafic minerals (Easton and Carter, 1995).

The three types of weathered/altered horizons presented here are all unconsolidated. Even when subjected to lithostatic loads of >20 MPa, these materials may retain their unconsolidated characteristics. One possible way to explain this may be that basement highs are acting as structural supports similar to pillars or columns, where unconsolidated weathered/altered materials in basement lows have pinched out, and stresses are supported at these basement contacts, effectively lessening the load on the materials between these highs.

Mineralized Contacts

Evidence for post-deposition or post-weathering mineralization at the contact is observed at Hidden Beach and Presque Isle in Marquette, Michigan, in the CPC BD-139 and CPC BD-151 cores, and at Cody, Wyoming. Dolomitized basement rock and iron-oxide mineralization of sedimentary and basement rocks are the primary types of mineralization seen at these sites. Significant iron-oxide mineralization (in which FeO is enriched by >5 wt% relative to host), and relatively high (<1000 ppm) concentrations of Ni and Cr, are observed at 3 locations at Presque Isle in the ultramafic basement host and the overlying sedimentary strata (Fig. 19b). Evidence for dolomitization is observed in the uppermost basement rocks in the CPC BD-139 core (Fig. b,d,e), (and likely the CPC BD-151 core, though this is solely supported by macroscopic observation) and in the Presque Isle serpentinized peridotite (Fig. 19f). Dolomitized basement rocks are defined by a >10 wt% enrichment of both CaO and MgO, relative to host rocks. Additionally, calcite, ankerite, and anhydrite exist in veins and slip surfaces in the basement rocks at Presque Isle and in the CPC BD-139 core (Table 1, Table 4). Calcite-cemented conglomerates and/or weathered horizons are also present at both sites in Marquette, Michigan, and at Cody, Wyoming (Figs. 19,22,33, Figs. 26-29).

Iron-Oxide Mineralization

Concentrated iron-oxide mineralization of the nonconformity zone is related to the presence of ultramafic basement rocks at Presque Isle. Significant iron-oxide mineralization is absent at Hidden Beach, where felsic basement rocks underlie the same basal sedimentary unit. Significant iron-oxide mineralization is also absent from all other sites examined in this project, particularly where the sedimentary units are underlain by felsic basement rocks. Ultramafic rocks are geochemically defined as low silica, high Fe-Mg-Mn igneous rocks (Sen, 2013), therefore it is likely that the serpentinized peridotite host rock at Presque Isle is the source of the iron-oxide mineralization.

Spatially, iron oxide mineralization of the nonconformity zone correlates with the presence of faults, occurring at 3 out of the 4 faulted sites (PI-S2, PI-S13, and PIS16) examined at Presque Isle, whereas all other sites do not contain significant iron oxide (Fig. 19-24). The host rocks and, in one case, the overlying Jacobsville Sandstone, at these 3 faulted are enriched in iron-oxide, indicating that an oxidizing fluid may have once flowed through the zones. The one faulted site that did not contain significant iron-oxide mineralization bisects the contact where the basal conglomerate is directly in contact with basement rock, and appears as a silica-rich lozenge-like vein in the basement, on which slip surfaces were observed (Fig. 21a). The lack of iron-oxide mineralization at this fault may be due to the relative permeability of the lozenge-like vein. It is possible that this structure acted as a barrier-type fault due to its tightly mineralized structure, inhibiting significant fluid flow, and thus iron-oxide mineralization, throughout the zone.

The presence of carbonate-mineralized contacts at sites with varying lithologies, specifically in gneisses, indicates that carbonate-mineralization of the nonconformity zone is independent of basement rock composition, and reflects alteration from an external source. At Hidden Beach, parts of the Jacobsville Sandstone basal conglomerate are cemented by calcite, and underlain by gneiss. Basement-hosted carbonate mineralization is widespread at Presque Isle, as calcite slip-surfaces, dolomite and calcite veins, and as patches of dolomitized host rock. At Cody, Wyoming, the laminated granitic wash is calcite-cemented, and crack-seal calcite veins are present in mafic basement-hosted fault gouge. In the CPC BD-139 core, dolomitized gneiss hosts calcite and anhydrite veins. Hydrothermal alteration in these rocks is supported by the presence of hydrothermally associated minerals in the CPC BD-139 core, such as zeolites, vermiculite, and clinochlore, therefore, we test a hydrothermal fluid source for our highest temperature scenario (Kerr, 1955) (Table 1).

Contact Types and Associated Seismic Risk

Contact scenarios associated with a low-risk injection environment (in which a low-permeability barrier exists at the contact) include well-cemented basal conglomerates, clayrich grus or granitic wash, and fully-mineralized horizons. High-risk injection environments (high-permeability nonconformity zones) include partially mineralized horizons and friable zones, such as poorly-cemented basal conglomerates, regolith, and clast-rich grus or granitic wash. Fault-sealing may occur due to faulting of the contact, depending on the degree of offset, whereas basement faults truncating at the contact may serve as flow conduits. Fracturing of these different contact types can greatly affect permeability, and therefore, associated seismic risk. The nature and density of fracture networks in the basement, as well as the mechanical properties of the materials at the contact, directly impact the hydrological connectivity of the contact zone. Mechanically strong horizons, such as a well-cemented conglomerate, may respond to stresses in a brittle manner, resulting in more abundant openmode fractures, whereas mechanically weaker materials, such as a clay-rich grus, may behave more ductilly, resulting in fewer hydrologically effective fracture networks (Ferrill et al., 2016).

Hydrologic Models of Saline Water Reinjection

We examine three-dimensional hydrogeologic models of brine re-injection within basal reservoirs proximal to crystalline basement faults and weathered zone using MODFLOW, a public domain groundwater flow model (Harbaugh et al. 2000; Harbaugh and McDonald 1996). We applied this model in a sensitivity study as well as at the Dagger Draw oil field in Southeastern NM. We are not aware of a weathered zone within the crystalline basement at Dagger Draw. This is a site where the USGS suspects that seismicity is triggered. We published a paper on triggered seismicity beneath the Dagger Draw oil field, Permian Basin in 2016 (Zhang et al. 2016). A manuscript on the sensitivity study is nearly complete (Ortiz et al. 2017) and will be submitted to the journal Ground Water in the next couple months. The MODFLOW code solves the following groundwater flow equation:

$$\frac{\partial}{\partial x} \left(K_x \frac{\partial h}{\partial x} \right) + \frac{\partial}{\partial y} \left(K_y \frac{\partial h}{\partial y} \right) + \frac{\partial}{\partial z} \left(K_z \frac{\partial h}{\partial z} \right)
= S_s \frac{\partial h}{\partial t} + Q(x, y, z, t)$$
(1)

where h is the hydraulic head [L], K is the hydraulic conductivity tensor [L t⁻¹], S_s is the specific storage [L⁻¹], Q is the fluid injection source term (i.e. injection well) [t⁻¹], and t is time [t]. Equation

(3) represents single-phase, constant-density groundwater flow in a three-dimensional, Cartesian coordinate system. Hydraulic conductivity (K) is a lumped parameter ($K = k\rho_f g / \mu$) that includes the influence of fluid properties (specific weight $\rho_f g$ and viscosity μ) and permeability (k) to transmit fluids. In the remainder of the paper, we will use permeability when referring to the transmissive properties of the rocks.

Sensitivity Study

We conducted a sensitivity study for a hydrogeologic system that considered basal reservoir injection adjacent to a fault zone (Fig. 36). We considered the presence/absence of a weathered zone as well (Ortiz, 2017).

Solution Schemes, Boundary, and Initial Conditions

The models were run for 19 years with a time step size of 2.5 hours for 1 day, subsequently increasing to 30 days for the remainder of the 19 years. We used a constant injection rate of 5000 m³ day-1 (roughly 1000 gpm). Although this injection rate is high for a single saline water injection well, it falls within the ranges used in other studies such as Keranen et al. (2014) near Jones, Oklahoma (four high-rate wells in that study had an injection rate of about 4 million barrels per month, which averages to $\sim 5,300$ m³ d⁻¹). A high injection rate is helpful to compare the order-of-magnitude pore pressure relationships at the wellhead and at depth within the crystalline basement. In all cases we placed the injection well within the reservoir 150 m from the fault zone, except for one where we tested the effect of increasing distance from the fault at 1 and 2 km spacing (Fig. 36).

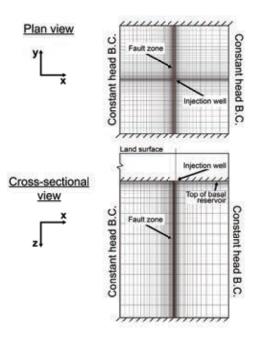


Fig. 36. MODFLOW model domain grid discretization and boundary conditions presented in (top) plan view, and (bottom) cross-sectional view. No-flux boundary on top of model domain simulates a very tight (i.e. non-leaky) confining unit overlain by a thick (~3 km) sequence of sedimentary rocks.

The model domain we used is 8 km by 8 km by 10 km (Fig. 36). The grid includes 64 columns, 74 rows, and 25 vertical layers (x, y, and z dimensions, respectively; 126,750 nodes). We used variable lateral and vertical spatial discretization (i.e. localized grid refinement) in order to more accurately resolve hydraulic head values near the fault zone, injection well, and the reservoir-basement interface. Horizontal grid discretization (Δx , Δy) was gradually increased from 10 to 630 m, with higher resolution close to the fault zone and increasing grid spacing towards the boundaries. Vertical discretization varied between 8 and 1000 m, with higher resolution near the reservoir-basement interface and increased spacing towards the base of the domain.

The fault zone represented in our models was varied between 30-150 m width. In all scenarios, the vertical fault zone extended to the bottom of the model domain. In some scenarios, the normal fault terminates at the reservoir-basement nonconformity: we refer to this as a Proterozoic fault (Fig. 37B). In other scenarios, the fault cuts through the reservoir (and altered zone, where present) in addition to the basement: we refer to this as a Paleozoic fault (Fig. 37). The different geologic units were vertically discretized (Δz) according to the relative importance of visualizing the vertical fluid pressure migration therein, as well as with consideration given to numerical effects such as grid dispersion. For example, the altered zone, which essentially acts as a confining unit between the injection horizon and underlying crystalline basement, was assigned multiple highly discretized grid layers despite its relative thinness. In doing so, it more accurately represents an aquitard by reducing the numerical grid dispersion that can occur if it were represented by a single layer. The uppermost (injection) horizon consists of two uniformly spaced layers totaling 80 m in thickness. The altered zone (when included for testing) is represented by five uniformly spaced layers between 1-20 m in total thickness. In one scenario, we represented a discontinuous (undulating) altered zone with discrete, 20-m-wide fault-parallel blocks such that the altered zone "pinches out" completely in evenly spaced intervals (Fig. 7). In this case, the altered zone does not directly affect the fault zone connecting the reservoir and basement fault zones (i.e. it does not "block" the fault zone). The underlying crystalline basement comprises the remaining layers, which increase in thickness from 8 to 1000 m with depth away from the reservoir-basement interface.

We imposed no-flux boundary conditions along the top and base of the model, as well as along the north and south lateral boundaries. The top of the model domain is intended to represent a basal reservoir overlain by a thick (~3 km) sequence of sedimentary rocks. We assume that the reservoir is overlain by a very tight (i.e. non-leaky, $k < 10^{-19}$ m²) confining unit such that there is no pore pressure leakage in the up-vertical direction. We have approximated this by imposing a no-flux boundary condition along the top surface. A noflux boundary allows heads to build up higher than they would otherwise, thus aiding in the visualization of pressure buildup. Constant head boundary conditions (h = 10,000 m) are enforced along the east and west lateral boundaries. This value was also the initial head value for all cells pre-injection. Since these boundaries are set far enough away from the injection well and fault zone, simulated head increases were not significantly affected by their presence. Their effect on the model results, which for injection scenarios is to cause pressures to effectively dissipate towards to the lateral boundaries without building up, is further tempered by the enforcement of the no-flux conditions mentioned earlier. The enforcement of the lateral no-flux boundary conditions is admittedly idealized in this regard; however, for the conceptual numerical model at hand, their presence allows us to visualize the order-of-magnitude relationships that exist for the different hydrogeologic scenarios modeled without introducing undue model complexity.

Fig. 37. Hydrogeologic framework used in sensitivity analysis (not to scale): (A) Unfaulted case, (B) Proterozoic conduit-barrier fault; (C) Paleozoic conduit-barrier fault; (D) Paleozoic conduit-barrier fault with a laterally continuous altered zone as a basal seal and also showing (inset) a discontinuous or undulating altered zone; and permeability architectural end-members: (E) conduit fault zone, and (F) barrier fault zone. Note that top of the model domain is intended to represent a confined basal reservoir overlain by thick (~3 km) sequence of sedimentary rocks (not shown).

Hydrogeologic Framework for Sensitivity Study

1 2

3

4

5

6

7

8

9

10

11

12

13

14

15

16

17

18

19

20

21

22

23

24

25

26

27

28

29

30

31

32

33

34 35 The base hydrogeologic configuration is characterized by a relatively thin (80-m thick) sedimentary layer into which fluid is injected (injection reservoir). The injection reservoir overlies thick (≥ 9.9 km) crystalline basement. In some cases, a very thin (1-20 m) altered zone lies at the reservoir-basement interface and serves as an aquitard underlying the injection reservoir. A vertical, planar fault cuts the model domain in half and spans its width entirely; its geometry lends itself to interpretation as a high-angle normal fault zone, the thickness and vertical extent of which is variable depending on the model case.

We consider a range of permeabilities for the altered zone and individual fault-zone components in this sensitivity study (Table 6). The fault is assumed to be either: (a) not present, (b) a Proterozoic fault hosted solely in the crystalline basement, or (c) a Paleozoic fault hosted in the basement and further cutting the injection reservoir and altered zone (where present). Throw on the fault is assumed to be negligible. The fault is represented in the model as one of the three conceptualized fault-zone archetypes: (1) conduit, characterized by elevated permeability compared to the undeformed host rock, (2) barrier, represented by reduced permeability, and (3) conduit-barrier, comprising a core region of low permeability surrounded by the highly permeable damage zone. In the first two cases, the permeability of all cells across the fault-zone's breadth are homogeneous; the conduitbarrier case is represented by a single low-permeability central cell and high-permeability cells on either side. The individual cell permeabilities of hydrogeologic units are generally treated as isotropic in this study, with the exception of one simulation aimed to produce a conduit-barrier fault zone by assigning bulk anisotropic properties. For the case of calculating effective anisotropy of the conduit-barrier fault zone used in this study, we use averaging equations for the effective permeability normal and parallel to the fault (x-axis, zaxis, respectively):

$$\hat{k}_{\perp} = \frac{b_T}{\sum_{i=1}^n \frac{b_i}{k_i}} \qquad \hat{k}_{\parallel} = \frac{\sum_{i=1}^n b_i k_i}{b_T},$$
 (2)

where k is effective permeability for either the fault-orthogonal (k_{\perp}) or fault-parallel (k_{\parallel}) direction, k_{\parallel} is the fault element width, k_{\parallel} is the number of fault elements (2, in our case), and subscript k_{\parallel} refers to the respective fault element. These relationships are based on fluid mass balance vis-à-vis Darcy's Law. For flow parallel to the fault plane (k_{\parallel}) , the effective permeability is controlled by the higher-permeability damage zone. For flow perpendicular (across) the fault plane, the low-permeability core has the biggest effect on k_{\perp} .

Table 6. Permeability (in m²) values varied in sensitivity study.

Model Run	Altered zone k	Fault age	Fault Perm. Structure	Damage zone k (res., a.z., bsmt.)	Core k (res., a.z., bsmt.)	Bulk Fault Zone Perm. (k _x , k _z)
1		_	_	_		_
2	-	Prot.	conduit- barrier			_
3	_	Pz	conduit- barrier	3 × 10 ⁻¹⁰ 3 × 10 ⁻¹⁴	3 × 10-16 — 3 × 10-16	_
4	_	Pz	barrier	_	_	3×10^{-18} 3×10^{-18}
5	_	Pz	conduit- barrier	_	_	3×10^{-15} 3×10^{-13}
6	_	Pz	conduit	_	_	3×10^{-14} 3×10^{-14}
7	_	Pz	conduit	_	_	3×10^{-14} 3×10^{-14}
8	3 × 10 ⁻¹⁸	Pz	conduit- barrier	3×10^{-10} 3×10^{-18} 3×10^{-14}	3×10^{-16} 3×10^{-19} 3×10^{-16}	-

Abbreviations: *k*, permeability; res., injection reservoir; a.z., altered zone; bsmt., basement; Prot., Proterozoic; Pz, Paleozoic.

Effect of Fault-Zone Architecture

We first consider the effects of representing Proterozoic and Paleozoic fault zones that include core and damage zones. The crystalline basement permeability in all scenarios is 3 × 10⁻¹⁷ m². Calculated heads presented in Fig. 38 (cross section view) and 39 (plan view) after four years of continuous injection indicate that the depth and horizontal pattern of excess pore pressure propagation is strongly controlled by fault zone properties (Table 6). The injection well is located 150 m from the fault zone within the injection reservoir. Cross-sectional results (Fig. 38) are presented

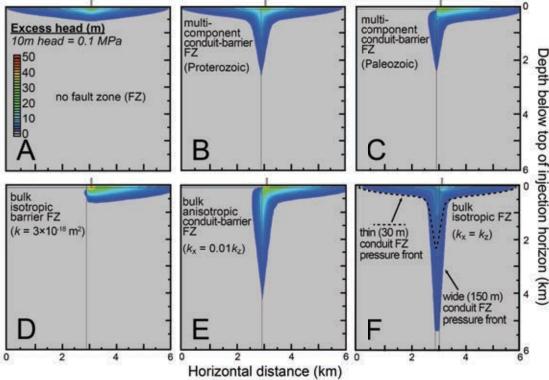


Fig. 38. Cross-sectional views of pore pressure envelope propagation after 4 years of constant-rate injection with no altered zone. Simulations presented are: (A) Unfaulted (B) Proterozoic conduit-barrier fault zone (C) Paleozoic conduit-barrier fault zone, (D) Paleozoic barrier fault zone assigned bulk isotropic properties ($k_x = k_{\chi} = 3 \times 10^{-18} \text{ m}^2$), (E) Paleozoic conduit-barrier fault zone assigned bulk anisotropic permeabilities (basement $k_x = 3 \times 10^{-15} \text{ m}^2$, $k_{\chi} = 3 \times 10^{-13} \text{ m}^2$), and (F) Paleozoic conduit fault zones assigned bulk isotropic permeabilities (basement $k_x = k_{\chi} = 3 \times 10^{-14} \text{ m}^2$), both for a thin (30-m-wide) fault zone (dashed line) and a thick (150-m-wide) fault zone. Results are zoomed in to the top 6 km × 6 km of the model domain. Vertical gray lines indicate location of the fault zone, and horizontal gray line denotes the reservoir-basement interface. Injection takes place 150 m to the right of the fault zone within the reservoir. Injection well location indicated on top of each panel. Transition from gray to dark blue contour (and all subsequent contour lines) denotes a 2 m increase in hydraulic head (0.02 MPa).

For a transect running perpendicular to the fault trace and in line with the injection well for maximum visibility of pressure increases. None of these scenarios in Fig. 38 and 39 consider an altered zone; that is, the 80-m-thick injection horizon rests unconformably on crystalline basement rock. Absent a fault zone, the 2-meter head (0.02 MPa) envelope extends to ~600 m depth, diffusing roughly 500 m into the crystalline basement rock (Fig. 38A). The deepest penetration of excess heads occurs directly under the injection well. The introduction of a 30-m-wide Proterozoic conduit-barrier fault zone (i.e. basement fault terminates at basement-reservoir interface) created a sizeable down-flow zone within the basement (to depths of ~2500 m) for fault damage zone permeability 3 orders of magnitude greater than the undeformed basement protolith (where basement $k_x = k_z = 3 \times 10^{-17}$ m²) and 2 orders of magnitude less permeable than the overlying injection reservoir rock (where $k_{reservoir} = 3 \times 10^{-12}$ m²), yet there was still

80

81

82

83

84

85

86

87

88

89

90

91

92

93

94

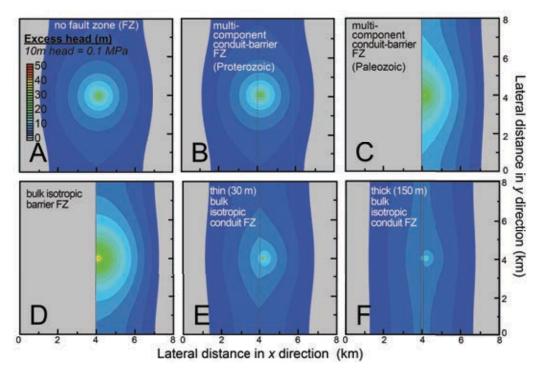


Fig. 39. Plan view of pore pressures – within the injection reservoir layer – spanning the entire lateral model domain (8 km × 8 km) after 4 years of constant-rate injection with no altered zone (A) no fault zone, (B) Proterozoic conduit-barrier fault zone, (C) Paleozoic conduit-barrier fault zone, (D) Paleozoic barrier fault zone assigned bulk isotropic properties ($k_x = k_z = 3 \times 10^{-18} \text{ m}^2$), (E) thin (30-m-wide) Paleozoic conduit fault zone, and (E) wide (150 m) Paleozoic conduit fault zone. Both conduit fault zones were assigned bulk isotropic permeabilities (basement FZ $k_x = k_z = 3 \times 10^{-14} \text{ m}^2$). Injection takes place 150 m to the right of the fault zone within the reservoir. Transition from gray to dark blue contour (and all subsequent contour lines) denotes a 2-m increase in hydraulic head (0.02 MPa).

significant buildup of pore pressures down the fault zone (i.e. head perturbations propagated to the left of the fault zone; Fig. 38 and 39). The fault core permeability is 3 × 10⁻¹⁶ m², 4 orders of magnitude less permeable than the undeformed reservoir rock and 1 order of magnitude more permeable than the crystalline basement. A simulation of a Paleozoic conduit-barrier fault (i.e. basement fault cuts into overlying injection reservoir rock) produced an excess pore pressure envelope extending to depths of ~2300 m. There is significant flow compartmentalization within the injection horizon (Fig. 38 and 39). With the injection well located just 150 m from the fault, elevated pore pressures on the order of 38 m (radius, r = 50 m) were able to build up in proximity to the well. For the Proterozoic fault, pore pressures increased to only 22 m measured at the same radial distance from the well (Fig. 38). The multiple architectural component (i.e. core, damage zone) fault zone scenarios considered in Fig. 38-C and Fig. 38A-C are compared to simulations wherein the fault zone was simply assigned bulk properties 38 and 39). (Fig.

Effect of Altered Zone

95

96

97

98

99

100

101

102

103

104

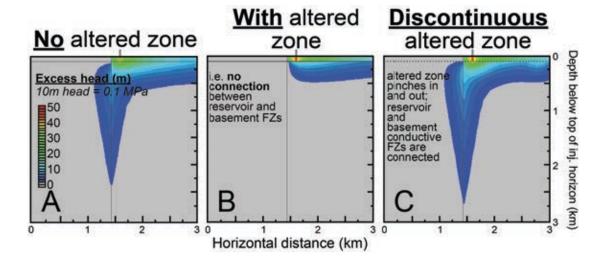
105

106

107

108 109 Because of the presence of laterally continuous altered zones at some outcrop analogs to modern basal reservoir injection sites, we felt it prudent to test the effect of such a layer on pore pressure migration. We compare simulations of a Paleozoic conduit-barrier fault with properties identical to those presented in Fig. 38D, but we included a 20-m-thick, low-permeability ($k_x = k_{\chi} = 3 \times 10^{-18}$ m²) altered zone; this is 1 order of magnitude less permeable than the basement host rock

We simulated a spatially heterogeneous altered zone that pinches and swells discretely along the nonconformity in 20-m-wide intervals (similar to the conceptual diagram in Fig. 37D inset) in order to test the effect of laterally discontinuous confining layer. The fault zone was not blocked by the altered zone, and elevated pore pressures propagated downward to depths of 2.7 km (Fig. 40). Elevated fluid pressures appeared to be forced down other areas where the altered zone pinches out, such as towards the right-hand side of Fig. 40C.



110 111

112

113

114

115

116

117

118

119

120

121

122

123

Fig. 40. Cross-sectional views of pore pressure envelope propagation resulting from injection into a reservoir underlain by a low-permeability altered zone. Excess heads after 4 years of constant-rate injection are presented for a Paleozoic conduit-barrier fault scenario (A) absent an altered zone, and (C) with a discontinuous altered zone that pinches in and out in 20-m horizontal intervals (i.e. undulating) but where the reservoir and basement fault zones are fully connected. Note the compartmentalization of the reservoir by the fault core in both cases and relatively little downward pressure diffusion when a laterally continuous altered zone is present. When altered zone is discontinuous across the conductive fault zone, pressures build up higher within the reservoir and are focused downward along the fault. Results are zoomed in to the top 3 km × 3 km of the model domain. Vertical gray lines indicate location of the fault zone. Injection well location is indicated on top of each panel. Transition from gray to dark blue contour (and all subsequent contour lines) denotes 2-m increase in hydraulic head (0.02)MPa).

The Dagger Draw oil field lies on the edge of the Permian Basin in southeastern New Mexico. Production began in 1969 (Fig. 41A) primarily out of the Canyon (Missourian) and Cisco (Virgilian) Groups that, in the Dagger Draw field, consist of upper Pennsylvanian reefal limestones (Broadhead, 1999). The oil is stratigraphically trapped in this carbonate unit and overlain by low-permeability shales in the Permian Hueco Formation and underlain by the Barnett and Woodford shales (Fig. 41; Broadhead, 1999). There are currently 138 producing wells in the Dagger Draw field, down from a peak of 414 producing wells in 2001 (GoTech; New Mexico Oil Conservation Division database). About 2-3 times as much brine is produced as oil by volume (Fig. 43), generally appearing as brackish water with TDS contents between 4,000 and 10,000 mg/l and a maximum salinity in some areas as high as 309,000 mg/l (Balch and Muraleedharan, 2014).

Produced oil-field brine is primarily injected into the basal Ellenburger Group. There is also some injection of oil-field brines into the overlying Montoya, Fusselman and Wristen carbonate units. Within the Dagger Draw oil field, permitted wellhead injection pressures for these formations range between about 1,520 m and 1,670 m for reservoir depths ranging between 3.3 and 3.6 km (New Mexico Oil Conservation Division, 2016). The Ellenburger thickness in New Mexico ranges from about 1 to 70 m (Holtz and Kerans, 1992). Ellenburger Limestone thickness increases to the southeast in Texas (Fig. 42; Wright, 1979). Porosity varies from 0.01 to 0.2 with an average of about 0.06. Core permeability values range from 2 to 100 mD (10-15 to 10-13 m²; Loucks, 2003). The Ellenburger experienced multiple episodes of karstification and dolomitization which likely enhanced its effective formation permeability above core measurements (Cox et al., 1998; Broadhead, 1999). In our numerical sensitivity study, we assign permeabilities to the Ellenburger ranging from 10-14 to 10-12 m².

Initial oil and produced water production was low until the early 1990s when the field was redeveloped. Peak production was in 1996 and the field has seen declining production ever since. The Dagger Draw field initially consisted of two fields, Dagger Draw North (DDN) and Dagger Draw South (DDS; Fig. 41B). The fields were originally developed separately and were thought to have independent geologic boundaries. Low permeable Upper Pennsylvanian carbonates in the uppermost part of the Cisco section and the overlying Hueco Formation provide the top seal for the Upper Pennsylvanian reservoir at Dagger Draw. The Woodford Shale (Devonian) provides the top seal for the Wristen (Silurian) carbonates. Carbonate reservoirs in the Fusselman (Silurian; underlies the Wristen), the Montoya, and the Ellenburger limestones are self-sealed by impermeable carbonate strata within those units. The Hueco Formation, the Barnett and Woodford Shales with the intervening Lower Mississippian limestone form the top seal for the Ellenburger, Montoya, Fusselman and Wristen carbonate sequence in the Dagger Draw area.

We focus our analysis on 83 reinjection wells within 20 km of the seismicity in Eddy County, New Mexico. Oil and water production data was taken from New Mexico Oil Conservation Division reports (Annual Report of the New Mexico Oil and Gas Engineering Commission Inc., 1969-2003) as well as the GoTech database (2004-2013). Monthly production data of oil, gas and water were summed for all wells in each Township/Range section and then compared to the monthly earthquake frequency ($M_d > 2$; Fig. 43). For our modeling effort, the 83 individual oil field brine reinjection wells were lumped into 15 regions (injection nodes) by township and range. That is, the 83 injection wells were represented by consolidating them into 15 injection nodes in our model. For some injection nodes, peak re-injection rates of exceeded 1 million barrels per month

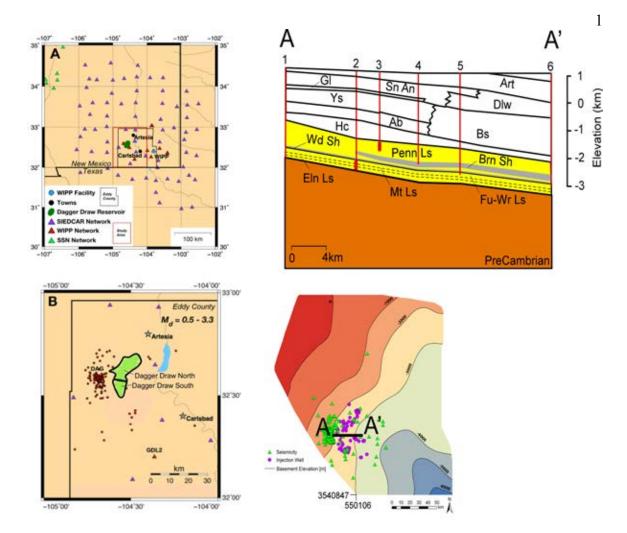


Fig. 41. (A) Study area map showing WIPP seismic (red triangles), SIEDCAR (purple triangles), Socorro Seismic Network (SSN, green triangles) location of the WIPP site and Dagger Draw (dark green blob) oil field in Eddy County, New Mexico. The location of the WIPP site is indicated by the blue circle. (B) Relocated epicenters (small red circles) for 203 earthquakes between 2008/09-2010/07 relative to the location of the Dagger Draw oil field. Oil field locations (green shaded areas) are courtesy of the New Mexico Bureau of Geology, reservoir outline from Speer (1993)

Fig. 42. Contour map of crystalline basement elevation (in m, sea level datum) surrounding the Dagger Draw oil field in southeastern NM. The locations of the 83 oil-field brine reinjection wells (purple circles) and seismicity (green triangles) are shown on the contour map. A geologic cross-section across the Dagger Draw oil filed is also shown. Oil production occurs primarily within Pennsylvanian carbonates (Penn Ls, yellow). Oil-field-brine reinjection occurs in the basal Ellenberger Group (El), Montoya Limestone (Mt), and Fusselman and Wristen limestone units (Fu-Ws, yellow). Additional geologic units include: Brn Sh, Barnett Shale (gray); Wd Sh, Woodford Shale (gray); Hc Hueco Formation; Ab Abo formation; Ys, Yeso Formation; Gl, Glorietta Sandstone; Sn An, San Adres formation; Art, Artesia Group.

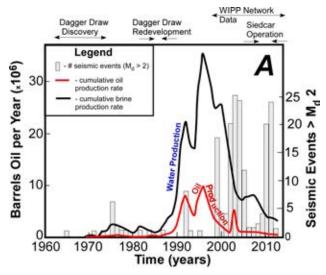


Fig. 43. Annual production of oil and saline brines (water) from the Dagger Draw Oil Field, Permian Basin and seismic events greater than M2.

The main goal of this modeling study was to assess what reservoir and crystalline basement permeability scenarios could produce a 5-year time lag of fluid pressure increases above 0.07 MPa (7 m of excess head) at a depth of 11 km in the crystalline basement to the west of the Dagger Draw oil field. A 7 m threshold for failure represents an intermediate value ascertained from prior studies.

We developed a three-dimensional hydrogeologic model to simulate injection into the Ellenburger Group at Dagger Draw (Fig. 44) and pressure diffusion into the crystalline basement using the United States Geological Survey's groundwater model, **MODFLOW** (Harbaugh McDonald, 1996). Bulk

crystalline basement permeability is related to the square of the aperture spacing of inter-connected fracture planes (Snow, 1968; Schwartz and Zhang, 2003). Because of the large spatial length scales represented in this study, it was not computationally possible to represent a distributed fracture network.

We used a uniform grid and represented a 5 order of magnitude contrast in hydraulic conductivity between the Ellenberger reservoir (0.86 m/day) and the Barnett Shale (0.000003 m/day; Fig. 44). Each finite difference cell had lateral dimensions of about 2.1 by 2.3 km (Δx by Δy , respectively). Vertical cell size varies considerably. We lumped the Barnett and Woodford Shales into a single 100 m-thick confining unit that was discretized using 5 layers ($\Delta z = 20$ m). We lumped the Ellenburger Montoya, Fusselman and Wristen carbonate units into a single layer. The layer thickness varied from 1 to 247 m with an average thickness of 85m. All injection took place in this layer. A total of 15 layers were used to represent the crystalline basement. The thickness of each crystalline basement layer varied from about 870 m to 1280 m.

Numerous studies argue that permeability decreases with depth (Manning and Ingebritsen, 1999; Stober and Bucher, 2007; Ingebritsen and Manning, 2010). In two scenarios, we allowed crystalline-basement permeability to decay with depth using the relationship presented by Manning and Ingebritsen (1995) and Ingebritsen and Manning (2010):

$$k = 10^{-12-3.4log_{10}(d)}$$
 (3a)
 $k = 10^{-14-3.4log_{10}(d)}$ (3b)

$$k = 10^{-14 - 3.4 \log_{10}(d)} \tag{3b}$$

where k is permeability of the crystalline basement in m^2 and d is depth in km. Equation 2b is considered more applicable to stable continental crust while 2a is considered to be more representative of the crust in tectonically active regions. The Permian Basin in SE New Mexico is considered to be a tectonically stable region. It is unclear whether or not elevated fluid pressures associated with brine re-injection could have a similar effect on seismicity as elevated tectonic stresses.

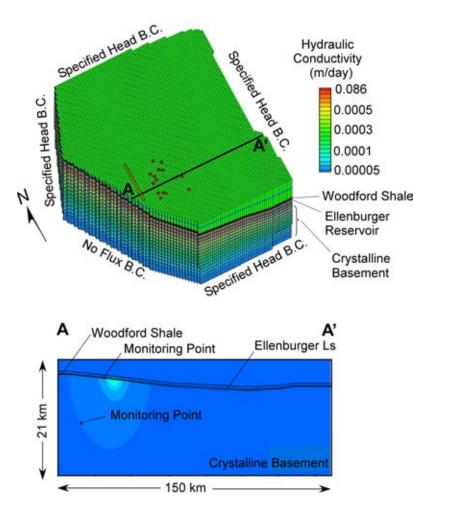


Fig. 44. Three dimensional view of MODFLOW finite difference grid and the East-West cross section A-A' showing locations of two monitoring points used in sensitivity study. The red squares denote the lateral position of the reinjection wells within the Ellenburger Limestone (layer 9) projected up onto the top layer. The thin orange line denotes the lateral position of a fault zone with relatively high permeability within the crystalline basement projected up onto the top layer (layers 10-25).

We also considered the presence of a vertical conductive fault (between 10⁻¹⁴ to 10⁻¹⁵ m²) centered in the region of increased seismicity (Fig. 45A, 45B, 45E, 45F). The fault zone was surrounded by a lower-permeability crystalline basement (10⁻¹⁶ m²). As noted above, it is plausible that the clustering of earthquake epicenters along a north-south region may be indicative of a wide conductive fault zone.

The presence of a permeable fault zone surrounded by a lower-permeability crystalline basement matrix (10-16 m²) facilitated the propagation of elevated pore pressures downward along the fault to the base of the model domain. The pressure anomaly extended outwards perpendicular to the fault zone (Fig. 45A, 45B, 45E, 45F). The depth of propagation of the pressure front in the fault zone is sensitive to fault permeability (compare Fig. 45A to 45B). Using a fault permeability of 10-14 m²



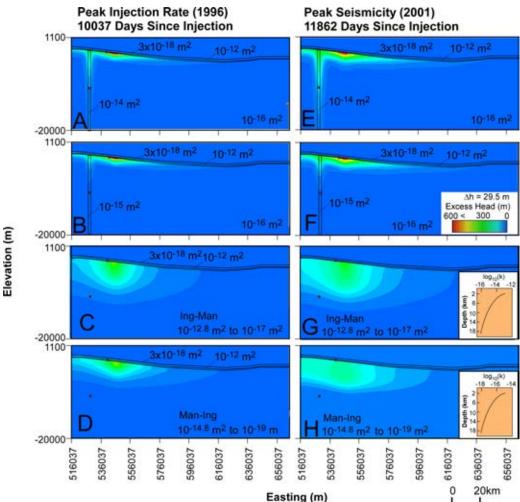


Fig. 45. Sensitivity study showing effect of changes in crystalline basement permeability on computed excess heads during peak injection (left column) and peak seismicity (right column). The reservoir permeability in all of these simulations was set at 10^{-12} m² (1000 mD). The following scenarios are considered here: a high permeability (10^{-14} m²) crystalline basement fault, Fig.s A & E; a low permeability (10^{-15} m²) crystalline basement fault, B & F; Ingebritsen and Manning (2010) permeability decay with depth imposed within the crystalline basement, C & G; Manning and Ingebritsen (1999) permeability decay with depth imposed within the crystalline basement, D & H. Vertical exaggeration is 3. The first head contour is 7 m. Subsequent contour intervals are 29.5 m (i.e. 7 m, 36.5 m, 66 m, 95.5 m, 125 m).

allowed the pressure front to propagate downward to a depth of 11 km relatively quickly. For this scenario, excess heads exceeded the 7 m threshold even before peak injection occurred (Fig. 46). Had we used a critical head threshold of 50 m, this scenario would have produced a 5-year lag between peak injection and seismicity. Using a fault permeability one order of magnitude lower (10⁻¹⁵ m²) resulted in modest head increase of less than 1 m during the simulation period (Fig. 46). We also ran one additional scenario setting the fault permeability equal to $3x10^{-15}$ m². This intermediate fault permeability scenario was able to reproduce both the 5-year lag and the 7 MPa pressure increase.

Next, we explored two scenarios of permeability decreasing with depth. In the first scenario, the permeability decayed from 10^{-12.8} to 10^{-17.3} m² (Fig. 45C, 45G). This scenario is consistent with crustal rocks in tectonically active regions (Ingebritsen and Manning, 2010) and we refer

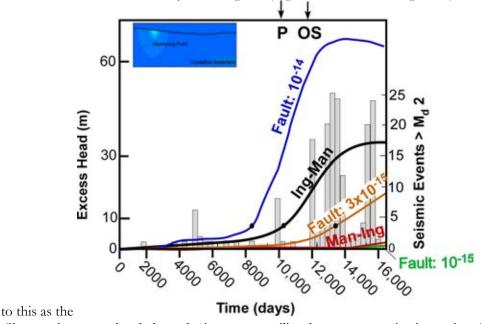


Fig. 46. Changes in excess head through time at crystalline basement monitoring point shown in inset. Lines show simulated excess heads for different basement permeability scenarios including the presence of a high permeability (10^{-14} m²) fault zone (blue), permeability decay with depth using the relationship presented by Ingebritsen and Manning (2010) (black), the presence of a relatively low permeability (3×10^{-15} m²) fault zone (orange), permeability decay with depth using the relationship presented by Manning and Ingebritsen (1999) (red) and the presence of a low permeability (10^{-15} m²) fault zone (green). The bar graph represents the number of earthquakes each year from 1969 to 2013 with $M_d > 2$. The origin of the time axis is January 1, 1969. Peak injection (P) occurred after 10037 days (1996.5). The onset of increased seismic frequency (OS) began in 2001.

Ingebritsen-Manning (Ing-Man) scenario. In a second scenario, more consistent with a stable continental crust (Manning and Ingebritsen, 1999), the permeability was varied from 10^{-14.8} to 10^{-19.3} m² (Fig. 45d, 45h). We refer to this as the Manning-Ingebritsen scenario (Man-Ing). The Ingebritsen-Manning scenario (dynamic crust) permitted the propagation of pore pressures in excess of 7 m downward to the centroid of seismicity by 2001 (Figure 45G). This was not the case for the Manning-Ingebristen (stable crust) scenario (Fig. 45h). However, neither the Manning-Ingebritsen (Man-Ing, Fig. 46) nor the Ingebritsen Manning (Ing-Man, Fig. 46) crystalline basement permeability scenarios predicted head increases of 7 m 5 years after peak injection at the centroid of seismicity (Fig. 46). It is likely that some intermediate permeability-depth decay relationship in between those presented in Fig. 45 would result in a head change of 7 m, 5 years after peak injection at the centroid of seismicity.

Conclusions

We examined outcrop and core analogs of the sedimentary-Precambrian nonconformity in the central United States in order to investigate the range of rock properties that may exist within the contact zone, with the intent on determining the nature of fluid flow through the contact zone. Outcrops were studied in Marquette, Michigan, Cody, Wyoming, and the northeastern Wind River Range, Wyoming. Core study included the CPC BD-139 and CPC BD-151 cores from St. Clair County, Michigan, and the UPH-1 core, from Stephenson County, Illinois. We characterized the structure, lithology, mineralogy, and geochemistry of the rocks at each of these sites, where applicable.

We identified 3 major contact zone scenarios through characterization of these 5 main sites. These are: 1) Basal conglomerate, 2) Weathered horizons (regolith, grus, granitic wash), and 3) Mineralized contact (carbonate and iron-oxide mineralization). Contacts with tight, well-cemented basal conglomerates may act as low-permeability barriers to flow or as a high-permeability conduit in the case of a friable, poorly-cemented conglomerate. Regolith and clay-poor/clast-supported grus or granitic wash at the contact likely acts as a high-permeability conduit. Clay-rich/matrix supported grus or granitic wash likely acts as a low-permeability barrier. Fully mineralized contacts may act as barriers to flow, whereas partially mineralized contacts may act as conduits to flow. The permeability of the contact may change over time with sustained brine injection due to fluid-rock interactions.

Identification of these zones may be possible with wire-line logging (spectral gamma, porosity, and sonic logs) or study of core if the borehole penetrates basement. For wells that do not penetrate basement, information from neighboring boreholes, regional geology, basin history, or basement topography may be useful in predicting the type of contact present.

Hydrologic models of conductive fault zones represented by realistic architectural permeability structures are a viable mechanism for transmitting elevated fluid pressures from the basal injection horizon to considerable depths (~2.5 km) within crystalline basement rock. We suspect that such fault zones have the potential to readily allow elevated pore pressures to trigger slip in critically-stressed basement faults and cause large, damaging earthquakes far below the fluid injection horizon. We hypothesize hydromechanical failure caused by excess pressures to be a potential mechanism for triggering deeper induced events (6-10 km) and confirm this process to greatly increase the depth of pressure front propagation. From a hazard mitigation standpoint, we note the effectiveness of even a thin (5-20 m), laterally continuous altered zone layer at the reservoir-basement interface in hindering the downward propagation of elevated pore pressures that could be transmitted by conductive faults. However, until more field and core log observations confirm both the ubiquity and lateral continuity of this distinct hydrogeologic unit, its inclusion in hydrogeologic models should be contingent on site-specific observations and be modeled accordingly.

Hydrologic modeling was used to in this study to test the hypothesis that increased rates of seismicity at 11 km depth within the crystalline basement 15 km west of the Dagger Draw oil field is the result of saline water injection into the basal Ellenburger reservoir. We considered several scenarios including assigning an effective or bulk permeability value to the crystalline basement, including a conductive fault zone surrounded by tighter crystalline basement rocks, and allowing permeability to decay with depth. We found that the observed lag-time between peak injection in 1996 and the onset of increase seismicity in 2001 can be explained by the time required for the pressure front to migrate through the crystalline basement. We assumed a 7 m head increase as a threshold for induced seismicity. The 5-year lag time helps constrain the permeability of the crystalline basement. If the crystalline basement was assigned a bulk permeability higher than 10^{-15} m², then delay between peak injection and seismicity would have been shorter than 5 years. Choosing a bulk permeability

less than 10⁻¹⁶ m² would not permit pressures to build sufficiently to induce seismicity. If a permeable fault-zone is present, its permeability needs to be about 3x10⁻¹⁵ m².

References

Annual Report of the New Mexico Oil and Gas Engineering Commission Inc., 1969-2003, Volume V I-A, southeastern New Mexico.

Barnes, D.A., Parris, T.M., and Grammer, M., 2008, Hydrothermal Dolomitization of Fluid Reservoirs in the Michigan basin, USA,

http://www.searchanddiscovery.com/pdfz/documents/2008/08075barnes/images/barnes.pdf.html (accessed March 2017).

Beaudoin, N., Leprêtre, R., Bellahsen, N., Lacombe, O., Amrouch, K., Callot, J.-P., Emmanuel, L., and Daniel, J.-M., 2012, Structural and microstructural evolution of the Rattlesnake Mountain Anticline (Wyoming, USA): New insights into the Sevier and Laramide orogenic stress build-up in the Bighorn Basin: Tectonophysics, v. 576–577, p. 20–45, doi: 10.1016/j.tecto.2012.03.036. Bell, L.H., and Middleton, L.T., 1978, An Introduction to the Cambrian Flathead Sandstone, Wind River Basin, Wyoming; Resources of the Wind River Basin: Wyoming Geological Association, 30th Annual Field Conference, Guidebook, p. 79–88.

Bowen, B.B., R.I. Ochoa, N.D. Wilkens, J. Brophy, T.R. Lovell, N. Fischietto, C.R. Medina, and J.A. Rupp. 2011, Depositional and Diagenetic Variability within the Cambrian Mount Simon Sandstone: Implications for Carbon Dioxide Sequestration: Environmental Geosciences v. 18, p. 69-89, doi:10.1306/eg.07271010012.

Brace, W. F. "Permeability of Crystalline Rocks: New in Situ Measurements." Journal of Geophysical Research: Solid Earth 89, no. B6 (June 10, 1984): 4327–30. doi:10.1029/JB089iB06p04327. Broadhead, R. F., 1999, Underdeveloped oil fields – Upper Pennsylvanian and Lower Wolfcampian carbonate reservoirs of southeast New Mexico, Carbonates and Evaporites, v. 14(1), pp. 84-105.

Calais, E., Han, J.Y., DeMets, C., and uet, J.M., 2006, Deformation of the North American Plate interior from a decade of continuous GPS measurements: Journal of Geophysical Research, v. 111, doi: http://dx.doi.org.dist.lib.usu.edu/10.1029/2005]B004253.

Cercone, K.R., 1984, Thermal History of Michigan Basin: America Association of Petroleum Geologists Bulletin, v. 68, p. 130–136.

Clayton, L., and Attig, J.W., 1990, Geology of Sauk County, Wisconsin: Wisconsin Geological and Natural History Survey Information Circular 67, http://www.koubadrilling.com/well-drilling/docs/sauk-county-geological-report.pdf (accessed July 2017).

Clayton, R.N., Friedman, I., Graf, D.L., Mayeda, T.K., Meents, W.F., and Shimp, N.F., 1966, The origin of saline formation waters; Part 1, Isotopic composition: Journal of Geophysical Research, v. 71, p. 3869–3882.

Coates, M.S., Haimson, B.C., Hinze, W., and Van Schmus, W.R., 1983, Introduction to the Illinois deep hole project: Journal of Geophysical Research, v. 88, p. 7267–7275.

Cobbold, P.R., Zanella, A., Rodrigues, N., and Løseth, H., 2013, Bedding-parallel fibrous veins (beef and cone-in-cone): Worldwide occurrence and possible significance in terms of fluid overpressure, hydrocarbon generation and mineralization: Marine and Petroleum Geology, v. 43, p. 1–20, doi: 10.1016/j.marpetgeo.2013.01.010.

Coniglio, M., R. Sherlock, A. E. Williams-Jones, K. Middleton, and S. K. Frape. "Burial and Hydrothermal Diagenesis of Ordovician Carbonates from the Michigan Basin, Ontario, Canada." In Dolomites, edited by Bruce Purser, urice Tucker, and Donald Zenger, 231–54. Blackwell Publishing Ltd., 1994. doi:10.1002/9781444304077.ch14.

Cooley, Maurice E. "Artesian Pressures and Water Quality in Paleozoic Aquifers in the Ten Sleep Area of the Bighorn Basin, North-Central Wyoming." U.S. Geological Survey Water-Supply Paper. Department of the Interior, 1986. https://pubs.usgs.gov/wsp/2289/report.pdf.

Cox, D. M., Brinton, L., and Tinker, S. W., 1998, Depositional facies and porosity development of an upper Pennsylvanian algal mound reservoir, south Dagger Draw, Eddy County, New Mexico, Cored

reservoir examples from Upper Pennsylvanian and Lower Permian carbonate margins, slopes and basinal sandstones, West Texas Geological Society, v. 98-103, variously paginated.

Crone, A.J., De Martini, P.M., Machette, M.N., Okumura, K., and Prescott, J.R., 2003,

Paleoseismicity of two historically quiescent faults in Australia; implications for fault behavior in stable continental regions: Bulletin of the Seismological Society of America, v. 93, p. 1913–1934.

Denison, R.E., Lidiak, E.G., Bickford, M.E., and Kisvarsanyi, E.B., 1984, Geology and

geochronology of Precambrian rocks in the Central Interior region of the United States: U.S. G.P.O., Professional Paper USGS Numbered Series 1241–C, http://pubs.er.usgs.gov/publication/pp1241C (accessed June 2017).

Dixon, T.H., Mao, A., and Stein, S., 1996, How rigid is the stable interior of the North American Plate? Geophysical Research Letters, v. 23, p. 3035–3038, doi:

http://dx.doi.org.dist.lib.usu.edu/10.1029/96GL02820.

Domrois, S., Marshak, S., Abert, C.C., and Larson, T.H., 2015, ArcGIS Maps Depicting Topography of the Basement-Cover Contact (the Great Unconformity), and the Traces of Faults and Folds, in the Cratonic Platform of the United States: American Association of Petroleum Geologists Search and Discovery Article #30410.

Dott, R. H., 1974, Cambrian Tropical Storm Waves in Wisconsin: Geology v. 2, p. 243-46.

Dott, R.H., and Attig, J.W., 2004, Roadside Geology of Wisconsin: Mountain Press Pub., 368 p. Duffin, M.E., 1989, Nature and origin of authigenic K-feldspar in Precambrian basement rocks of the North American midcontinent: Geology, v. 17, p. 765–768, doi: 10.1130/0091-7613(1989)017<0765:NAOOAK>2.3.CO;2.

Duffin, M.E., Lee, M., Klein, G. deVries, and Hay, R.L., 1989, Potassic diagenesis of Cambrian sandstones and Precambrian granitic basement in UPH-3 deep hole, Upper Mississippi Valley, U.S.A.: Journal of Sedimentary Research, v. 59, p. 848–861, doi: 10.1306/212F908E-2B24-11D7-8648000102C1865D.

Dutton, Clarence Edward. Tertiary History of the Grand Canon District. University of Arizona Press, 1882.

Easton, R.M., and Carter, T.R., 1995, Geology of the Precambrian Basement Beneath the Paleozoic of Southwestern Ontario, in Ojakangas, R.W., Dickas, A.B., and Green, J.C. eds., Basement Tectonics 10, Springer Netherlands, Proceedings of the International Conferences on Basement Tectonics, v. 4, p. 221–264, doi: 10.1007/978-94-017-0831-9 26.

Edel, S., 2015, Characterizing suspected induced seismicity in SE New Mexico in the vicinity of the Waste Isolation Pilot Plant, NM Tech MSc Thesis, 91 p.

Ellsworth, W.L., 2013, Injection-Induced Earthquakes: Science, 341, p. 142, doi: 10.1126/science.1225942.

Environmental Protection Agency, and Underground Injection Control, 2015, Class II Oil and Gas Related Injection Wells: United States Environmental Protection Agency,

https://www.epa.gov/uic/class-ii-oil-and-gas-related-injection-wells (accessed June 2017).

Evans, J.P., Berry, M., Allred, I., Nielson, K., and Parslow, D., 2013, How many Class II wells present a risk for induced seismicity?,

https://gsa.confex.com/gsa/2013AM/webprogram/Paper226615.html

Everham, W.D., and Huntoon, J.E., 1999, Thermal history of a deep well in the Michigan Basin; implications for a complex burial history (A. Foerster, Ed.): Kluwer Academic/Plenum Publishers; New York; NY,

http://search.proquest.com.dist.lib.usu.edu/georef/docview/52420903/D1E9596410E24127PQ/1 (accessed March 2017).

Faure, G., 2009, Isotopes: Principles and Applications: John Wiley & Sons, 897 p.

Ferrill, David A., Alan P. Morris, Sarah S. Wigginton, Kevin J. Smart, Ronald N. McGinnis, and Daniel Lehrmann. "Deciphering Thrust Fault Nucleation and Propagation and the Importance of Footwall Synclines." Journal of Structural Geology 85, no. Supplement C (April 1, 2016): 1–11. doi:10.1016/j.jsg.2016.01.009.

Frailey, Scott M., James Damico, and Hannes E. Leetaru. "Reservoir Characterization of the Mt. Simon Sandstone, Illinois Basin, USA." Energy Procedia, 10th International Conference on Greenhouse Gas Control Technologies, 4, no. Supplement C (January 1, 2011): 5487–94. doi:10.1016/j.egypro.2011.02.534.

Friedman, I., O'Neil, J.R., and Fleischer, M., 1977, U. S. Geological Survey Professional Paper: U. S. Geological Survey Professional Paper, p. 12.

Gair, J.E., and Thaden, R.E., 1968a, Geology of the Marquette and Sands Quadrangles, Marquette County, Michigan: Geological Survey Professional Paper 397,

https://pubs.usgs.gov/pp/0397/report.pdf (accessed March 2017).

Girard, J.-P., and Barnes, D.A., 1995, Illitization and Paleothermal Regimes in the Middle Ordovician St. Peter Sandstone, Central Michigan Basin: K-Ar, Oxygen Isotope, and Fluid Inclusion Data: American Association of Petroleum Geologists Bulletin, v. 79, p. 49–69.

Granger, H.C., McKay, E.J., Mattick, R.E., Patten, L.L., and McIlroy, P., 1971, Mineral resources of the Glacier Primitive Area, Wyoming: U.S. Govt. Print. Off., Bulletin USGS Numbered Series 1319–F, http://pubs.er.usgs.gov/publication/b1319F (accessed July 2017).

Hamblin, W.K., 1958, The Cambrian sandstones of northern Michigan. [Ph.D. Dissertation]: University of Michigan, 55 p. Michigan Geological Survey Publication #51.

Harbaugh, Arlen W., and Michael G. McDonald, 1996, *User's documentation for MODFLOW-96, an update to the US Geological Survey modular finite-difference ground-water flow model.* No. 96-485. US Geological Survey; Branch of Information Services [distributor].

Harrison, R.W., Hoffman, D., Vaughn, J.D., Palmer, J.R., Wiscombe, C.L., McGeehin, J.P., Stephenson, W.J., Odum, J.K., Williams, R.A., and Forman, S.L., 1999, An example of neotectonism in a continental interior - Thebes Gap, Midcontinent, United States: Tectonophysics, v. 305, p. 399-417, doi: 10.1016/S0040-1951(99)00010-4.

Heinrich, E. William. "Economic Geology of the Sand and Sandstone Resources of Michigan." Report of Investigation. Michigan Department of Environmental Quality, 2001.

http://www.michigan.gov/documents/deg/GIMDL-RI21 216264 7.pdf.

Hesseltine, G., Evans, J.P., Kerner, K., and Mozley, P.S., 2016, Structural diagenesis and micro-to macro-scale structural architecture of basal nonconformities, in Denver, CO, doi: 10.1130/abs/2016AM-284922.

Holtz, M. H., and Kerans, C., 1992, Characterization and classification of west Texas Ellenburger reservoirs, *in* Candelaria, M. P., and Reed, C. L., Eds., Paleokarst related diagenesis and reservoir development: Examples from Ordovician-Devonian age strata of west Texas and the mid-continent: Permian Basin Section SEPM 1992 Annual Field Trip, 45-54.

Ingebritsen, S. E., and Manning, C. E., 2010, Permeability of the continental crust: Dynamic variations inferred from seismicity and metamorphism. Geofluids, v. 10, pp. 193-205.

Kawano, Seiya, Ikuo Katayama, and Keishi Okazaki. "Permeability Anisotropy of Serpentinite and Fluid Pathways in a Subduction Zone." Geology 39, no. 10 (October 1, 2011): 939–42. doi:10.1130/G32173.1.

Keranen, K.M., Weingarten, M., Abers, G.A., Bekins, B.A., and Ge, S., 2014, Sharp increase in central Oklahoma seismicity since 2008 induced by massive wastewater injection: Science, v. 345, p. 448–451, doi: http://dx.doi.org.dist.lib.usu.edu/10.1126/science.1255802.

Kerner, K.R., 2015, Permeability architecture of faulted nonconformities: Implications for induced seismicity [M.S.]: New Mexico Institute of Mining and Technology, 162 p.,

https://search.proquest.com/docview/1749295549/abstract/774D131EA2FF4426PQ/1 (accessed July 2017).

Kerner, K., Mozley, P., Evans, J., and Person, M., 2015, Geologic Controls on Injection Related Reactivation of Basement Faults, in Denver, CO,

http://www.searchanddiscovery.com/abstracts/html/2015/90216ace/abstracts/2096068.html (accessed June 2017).

Kerr, P.F., 1955, Hydrothermal Alteration and Weathering: Geological Society of America Special Paper 62, p. 525–546.

Kharaka, Y.K., Ambats, G., Thordsen, J.J., and Davis, R.A., 1997, Deep well injection of brine from Paradox Valley, Colorado: Potential major precipitation problems remediated by nanofiltration: Water Resources Research, v. 33, p. 1013–1020, doi: 10.1029/97WR00573.

Kim, W.-Y., 2013, Induced seismicity associated with fluid injection into a deep well in Youngstown, Ohio: Journal of Geophysical Research: Solid Earth, v. 118, p. 3506–3518, doi: 10.1002/jgrb.50247. Kim, S.-T., Coplen, T.B., and Horita, J., 2015, Normalization of stable isotope data for carbonate minerals: Implementation of IUPAC guidelines: Geochimica et Cosmochimica Acta, v. 158, p. 276–289, doi: 10.1016/j.gca.2015.02.011.

Kolata, D.R., 2005, Bedrock geology of Illinois: Illinois State Geological Survey Illinois Map 14 Bedrock Geologic Map, https://ngmdb.usgs.gov/Prodesc/proddesc_87181.htm (accessed May 2017).

Lewan, M.D., 1972, Metasomatism and weathering of the Presque Isle serpentinized peridotite, Marquette, Michigan [MSc. thesis]: Michigan Technological University, Houghton, MI, United States (USA), 48 p.

Ma, L., Castro, M.C., and Hall, C.M., 2009, Atmospheric noble gas signatures in deep Michigan Basin brines as indicators of a past thermal event: Earth and Planetary Science Letters, v. 277, p. 137–147, doi: http://dx.doi.org.dist.lib.usu.edu/10.1016/j.epsl.2008.10.015.

Manning, C. E., and Ingebritsen, S. E., 1999, Permeability of the continental crust: constraints from heat flow models and metamorphic systems. Reviews in Geophysics, v. 37, p. 127-150.

Marshak, S., Domrois, S., Abert, C., Larson, T., Pavlis, G., Hamburger, M., Yang, X., Gilbert, H., and Chen, C., 2017, The basement revealed: Tectonic insight from a digital elevation model of the Great Unconformity, USA cratonic platform: Geology, v. 45, p. 391-394.

Marshak, S., and Paulsen, T., 1996, Midcontinent U.S. fault and fold zones: A legacy of Proterozoic intracratonic extensional tectonism? Geology, v. 24, p. 151–154, doi: 10.1130/0091-7613(1996)024<0151:MUSFAF>2.3.CO;2.

Migon, P., and Thomas, M.F., 2002, Grus weathering mantles; problems of interpretation (B. J. Smith, Ed.): Catena, v. 49, p. 5–24.

Milstein, R., 1987, Bedrock Geology of Southern Michigan: Michigan Department of Natural Resources Geological Publication BG-01 Bedrock Geologic Map,

https://ngmdb.usgs.gov/Prodesc/proddesc_71887.htm (accessed May 2017).

Murray, K.E., 2015, Class II Saltwater Disposal for 2009-2014 at the Annual-, State-, and County-Scales by Geologic Zones of Completion, Oklahoma: Oklahoma Geological Survey Open-File Report OF5-2015, 18 p., http://ogs.ou.edu/docs/openfile/OF5-2015.pdf (accessed June 2017). Murray, K., 2016, Fluid Production and Injection Budget for the Arbuckle: Oklahoma, Final Report, Feb 2015–May 2016; https://scits.stanford.edu/murray-kyle-fluid-production-and-injection-budget-arbuckle-oklahoma-final-report-feb-2015-may-2016 (accessed June 2017).

National Research Council et. al., 2013, Induced Seismicity Potential in Energy Technologies: National Academies Press, Washington, D.C., 238 p.

National Technical Workgroup, and Underground Injection Control, 2014, Minimizing and Managing Potential Impacts of Injection-Induced Seismicity from Class II Disposal Wells: Practical Approaches: U.S. Environmental Protection Agency,

https://www.epa.gov/sites/production/files/2015-08/documents/induced-seismicity-201502.pdf (accessed July 2017).

New Mexico Oil Conservation Division, 2016,

http://ocdimage.emnrd.state.nm.us/imaging/AEOrderCriteria.aspx

O'Hanley, David S. "Solution to the Volume Problem in Serpentinization." Geology 20, no. 8 (August 1, 1992): 705–8. doi:10.1130/0091-7613(1992)020<0705:STTVPI>2.3.CO;2.

Ortiz, J., 2017, The Role of Fault-Zone Architectural Elements and Basal Regolith on Downward Pore Pressure Propagation and Induced Seismicity [MSc. thesis]: New Mexico Tech, Socorro, New Mexico, 45p.

Pain, C.F., 1991, Field Guide for Describing Regolith and Landforms: Australia, CRC LEME, c/o CSIRO Exploration and Mining, 108 p.

Peters, S.E., and Gaines, R.R., 2012, Formation of the "Great Unconformity" as a trigger for the Cambrian explosion: Nature (London), v. 484, p. 363–366, doi:

http://dx.doi.org.dist.lib.usu.edu/10.1038/nature10969.

Pettijohn, F.J., Potter, P.E., and Siever, R., 2012, Sand and Sandstone: Springer Science & Business Media, 560 p.

Ramsay, John G. "The Crack-seal Mechanism of Rock Deformation." Nature 284, no. 5752 (March 13, 1980): 135–39. doi:10.1038/284135a0.

Schwartz, F. W., AND Zhang, H., 2003, Fundamentals of Ground Water: John Wiley & Sons, New York, 583 p.

Sen, G., 2013, Petrology: Principles and Practice: Springer Science & Business Media, 371 p. Sharp, Z., 2007, Principles of Stable Isotope Geochemistry: Prentice Hall, 360 p.

Sloss, L. L., 1963, Sequences in the Cratonic Interior of North America: Geological Society of America Bulletin, v. 74, p. 93–114.

Snow, D. T., Fracture deformation and changes of permeability and storage upon changes of fluid pressure, Quart. Colo. Sch. Mines, 631, 201–244, 1968b.

Sorbie, K.S., and Mackay, E.J., 2000, Mixing of injected, connate and aquifer brines in waterflooding and its relevance to oilfield scaling: Journal of Petroleum Science and Engineering, v. 27, p. 85–106, doi: 10.1016/S0920-4105(00)00050-4.

Stober, I. and Bucher, K., 2007, Hydraulic properties of the crystalline basement, Hydrogeology Journal, 15: 213-224.

Stuckless, J.S., 1989, Petrogenesis of Two Contrasting, Late Archean Granitoids, Wind River Range, Wyoming: Professional Paper 1491, https://pubs.usgs.gov/pp/1491/report.pdf (accessed January 2017).

Tyrrell, J.P., Samuels, R.M., Low, P.C., and Anonymous, 2013, Management of produced water from oil and gas wells in California; past trends and future suggestions: Abstracts with Programs - Geological Society of America, v. 45, p. 595.

Urey, H.C., 1947, The thermodynamic properties of isotopic substances: Journal of the Chemical Society (Resumed), p. 562–581, doi: 10.1039/JR9470000562.

U.S. Geological Survey, 2017, Induced Earthquakes: Earthquake Hazards Program, https://earthquake.usgs.gov/research/induced/overview.php.

Vasconcelos, C., McKenzie, J.A., Warthmann, R., and Bernasconi, S.M., 2005, Calibration of the δ¹⁸O paleothermometer for dolomite precipitated in microbial cultures and natural environments: Geological Society of America, v. 33, p. 317–320.

Vitaliano, C.J., McCormick, G.R., Dahl, P.S., and Eckstein, Y., 1986, Granitic Rocks from Three Deep Drill-Holes, Illinois: The Journal of Geology, v. 94, p. 594–599.

Walsh, F.R., and Zoback, M.D., 2015, Oklahoma's recent earthquakes and saltwater disposal: Science Advances, v. 1, 9 p., doi: 10.1126/sciadv.1500195.

Weingarten, M., Ge, S., Godt, J.W., Bekins, B.A., and Rubinstein, J.L., 2015, High-rate injection is associated with the increase in U.S. mid-continent seismicity: Science, v. 348, p. 1336–1340, doi: 10.1126/science.aab1345.

Wilson, T.P., and Long, D.T., 1993, Geochemistry and isotope chemistry of Michigan Basin brines; Devonian formations: Applied Geochemistry, v. 8, p. 81–100, doi:

http://dx.doi.org.dist.lib.usu.edu/10.1016/0883-2927(93)90058-O.

Whitmeyer, S.J. and Karlstrom, K.E. 2007. Tectonic model for the Proterozoic growth of North America. Geosphere, 3, p. 220–259, doi: 10.1130/GES00055.1

Yeck, W.L., Weingarten, M., Benz, H.M., McNamara, D.E., Bergman, E.A., Herrmann, R.B., Rubinstein, J.L., and Earle, P.S., 2016, Far-field pressurization likely caused one of the largest injection induced earthquakes by reactivating a large preexisting basement fault structure: Geophy. Res. Lett., v. 43, p. 198-207, doi: 10.1002/2016GL070861

Zhang, Y., Edel, S.S., Pepin, J., Person, M., Broadhead, R., Ortiz, J.P., Bilek, S.L., Mozley, P., and Evans, J.P., 2016, Exploring the potential linkages between oil-field brine reinjection, crystalline basement permeability, and triggered seismicity for the Dagger Draw Oil field, southeastern New Mexico, USA, using hydrologic modeling: Geofluids, v. 16, p. 971–987, doi: 10.1111/gfl.12199. Zhang, Y., Person, M., Rupp, J., Ellett, K., Celia, M.A., Gable, C.W., Bowen, B., Evans, J., Bandilla, K., Mozley, P., Dewers, T., and Elliot, T., 2013, Hydrogeologic Controls on Induced Seismicity in Crystalline Basement Rocks Due to Fluid Injection into Basal Reservoirs: Groundwater, v. 51, p. 525–538, doi: 10.1111/gwat.12071.

Publications/Abstracts resulting from the work performed under the award

Cuccio, L.A., Evans, J. P., Bradbury, K. K., Mozley, P. S., 2016, Hydrological analysis of nonconformities: Implications for injection-induced seismicity in the midcontinent of the United States, Geol. Soc. Am. Annual Meeting abstract 171-2.

Cuccio, L. A., 2017, Geological characterization of Precambrian nonconformities: Implications for injection-induced seismicity in the midcontinent United States, Master's thesis, Utah State University, Logan, 131 p.

Hesseltine, G., 2017, Mineralization at the Precambrian-Paleozoic nonconformity and its implications for injection-related seismicity, , Master's thesis, Utah State University, Logan.

Hesseltine, G., Evans, J. P., Kerner, K., and Mozley, P. S., 2016, Structural diagenesis and micro-to macro-scale structural architecture of basal nonconformities, Geol. Soc. Am. Annual Meeting abstract 171-6.

Ortiz, J. P., Person, M., Mozley, P. S., and Evans, J. P., 2016, The hydrologic connection between basal reservoir injection, crystalline basement fault zones, and induced seismicity. Geol. Soc. Am. Annual Meeting abstract 201-8.

Ortiz, J, 2017, The Role of Fault-Zone Architectural Elements and Basal Regolith on Downward Pore Pressure Propagation and Induced Seismicity, MSc. Thesis, NM Tech.

Zhang, Y., Edel, S.S., Pepin, J., Person, M., Broadhead, R., Ortiz, J.P., Bilek, S.L., Mozley, P., and Evans, J.P., 2016, Exploring the potential linkages between oil-field brine reinjection, crystalline basement permeability, and triggered seismicity for the Dagger Draw Oil field, southeastern New Mexico, USA, using hydrologic modeling: Geofluids, v. 16, p. 971–987, doi: 10.1111/gfl.12199.